

Staircase resiliency in a fluctuating cellular array

F. R. Ramirez^{✉*} and P. H. Diamond^{✉†}

Department of Physics, University of California San Diego, La Jolla, California 92093, USA

 (Received 20 April 2023; revised 23 December 2023; accepted 8 January 2024; published 14 February 2024)

Inhomogeneous mixing by stationary convective cells set in a fixed array is a particularly simple route to layering. Layered profile structures, or staircases, have been observed in many systems, including drift-wave turbulence in magnetic confinement devices. The simplest type of staircase occurs in passive-scalar advection, due to the existence and interplay of two disparate timescales, the cell turn-over (τ_H), and the cell diffusion (τ_D) time. In this simple system, we study the resiliency of the staircase structure in the presence of global transverse shear and weak vortex scattering. The fixed cellular array is then generalized to a fluctuating vortex array in a series of numerical experiments. The focus is on regimes of low-modest effective Reynolds numbers, as found in magnetic fusion devices. By systematically perturbing the elements of the vortex array, we learn that staircases form and are resilient (although steps become less regular, due to cell mergers) over a broad range of Reynolds numbers. The criteria for resiliency are (a) $\tau_D \gg \tau_H$ and (b) a sufficiently high profile curvature ($\kappa \geq 1.5$). We learn that scalar concentration travels along regions of shear, thus staircase barriers form first, and scalar concentration "homogenizes" in vortices later. The scattering of vortices induces a lower effective speed of scalar concentration front propagation. The paths are those of the least time. We observe that if background diffusion is kept fixed, the cell geometric properties can be used to derive an approximation for the effective diffusivity of the scalar. The effective diffusivity of the fluctuating vortex array does not deviate significantly from that of the fixed cellular array.

DOI: [10.1103/PhysRevE.109.025209](https://doi.org/10.1103/PhysRevE.109.025209)

I. INTRODUCTION

A. Background

Staircases [1]—structures of long-range layered order [2]—have been predicted and observed in applications such as doubly diffusive convection (e.g., stellar interiors, oceans, and planetary atmospheres) [3,4], rotating geophysical fluids [e.g., potential vorticity (PV) jumps associated with sharp jets (zonal flows)] [1], fluids with stratified density [5], and magnetized plasmas [6–9]. In all of these, sharp gradient layers act as barriers to transport. On account that layering is observed in many different types of systems, it is beneficial to understand how staircases form—i.e., how “inhomogeneous mixing” is realized? Such mixing results in the local sharpening of a scalar’s (e.g., PV, temperature, etc.) gradient. When the gradient steepens, a pattern of “jumps” and “steps” develop in the scalar profile, hence the staircase.

In magnetically confined plasma, layering is manifested by the formation of an $\mathbf{E} \times \mathbf{B}$ staircase—a quasiperiodic pattern of mean field and fluctuation intensity. A signature of this structure is the containment of avalanche activity, which can be detrimental to confinement [10]. Both simulation and experimental data have shown a pressure profile that resembles a staircase. At “jumps” (strong localized temperature gradients), turbulence drives an enduring layer of localized shear that acts as a permeable transport barrier. In regions of

“steps” (mixing region), there is strong, avalanche-like transport. Here, the interspersed regions of localized shear reduce the spread of avalanche-like transport.

There are two common approaches when explaining the phenomenon of layering in magnetic confinement. One approach proposes that the formation process is due to the interplay of mixing on two length scales [11]. Here, bistability, which is key to staircase formation, enters via a gradient dependent mixing length. The mixing length is determined by an excitation scale and the Rhines scale [12]. The emergent scale for drift-wave turbulence is the Rhines scale [13,14], which is defined by the cross-over between the wave interaction mismatch frequency and the decorrelation rate characteristic of the inverse cascade. Note that both the local profile scale length and the turbulence intensity enter the Rhines scale—hence its “emergent” character. The interplay of processes on two length scales triggers self-sharpening of modulations, leading to a staircase. For an extensive study on the two-scale mixing process, see Refs. [15–18]. The other approach is the jams model [19–21]. In this alternative picture, the staircase forms due to a time delay between temperature modulations and local heat flux. For a more detailed discussion of these two approaches, see Appendix A.

So far, nearly all suggestions involve a feedback process between zonal shears, turbulence, and their mutual interaction by modulation processes. However, perhaps the *simplest* explanation of inhomogeneous mixing is to observe that it occurs when the turbulence field is organized in an array of marginally overlapping convective cells (see Fig. 1). Such a configuration is expected when instabilities are weakly

*f3ramire@ucsd.edu

†pdiamond@ucsd.edu

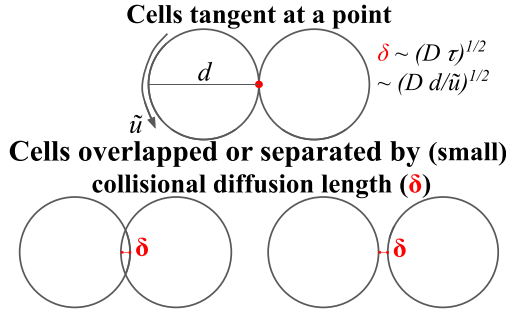


FIG. 1. Illustration of marginally overlapping cells. Marginally overlapping cells are cells that are tangent at a point, or which intersect over, or are separated by, a distance of no more than a collisional diffusion length.

excited but not strong enough to produce large transport (i.e., when turbulence is relatively weak, cells overlap only slightly, and profiles are “near-marginal”). Such states are characteristic of “stiff profiles”, which adopt roughly the same shape regardless of the applied heating and fueling profiles [22].

Marginally overlapping cells capture two different transport mechanisms. The two transport methods can be understood using the setup of overlapping and nearly overlapping cells (see Fig. 2). In the former, particles can scatter directly from cell to cell. A classic example of the latter is the problem of passive-scalar advection by an array of stationary convective cells [23–25]. A feature of this model is that there is a coexistence and interplay of fast (cell turn-over) and slow (diffusion) transport timescales. In this setup, many overturns occur in one diffusion time, thus resulting in inhomogeneous mixing. As depicted in Fig. 4, the system has a global density gradient in the x direction. As the cells rotate, they capture and trap particles. Due to a global diffusion D , the particles can be kicked off a streamline at a narrow gap (δ) between two convective cells. Note that we assume that the characteristic scale of the cells is d , hence $d \gg \delta$. Here, the cell boundary acts as a transport barrier; therefore, the *simplest* case of staircase formation occurs in a stationary array of eddies and passive scalar dynamics (see Fig. 3). It is important to note that in

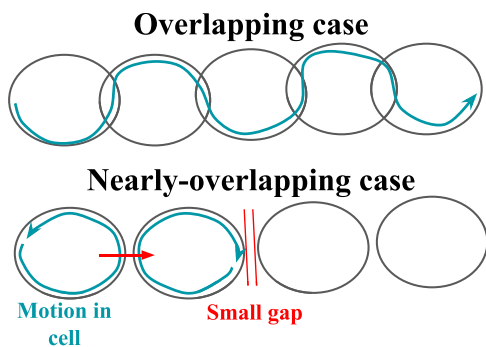


FIG. 2. Particle transport in overlapping and nearly overlapping cells. In the overlapping case, the particle can scatter directly from cell to cell. For the nearly overlapping case, there is a coexistence of fast transport (mixing in cell) and slow transport (kicks between cells).

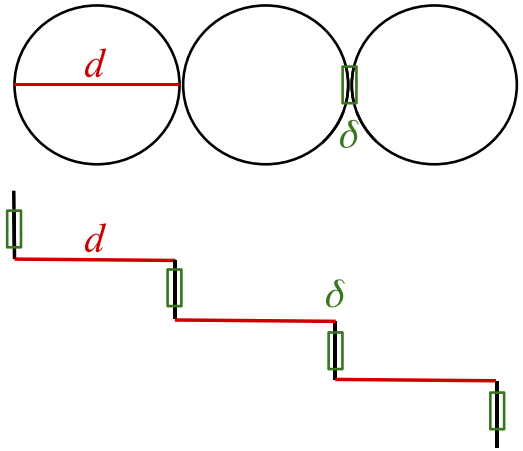


FIG. 3. Illustration of a staircase profile. Domains of cellular mixing (“steps”) and regions of cell boundaries (“jumps”) are denoted by d (red) and δ (green), respectively.

this setup, “feedback” is not necessary to form a staircase structure.

A remarkable result which is characteristic of this model is the effective diffusivity (D^*) caused by the interplay of fast and slow transport. To derive the effective diffusivity, we consider a random walk with a diffusion coefficient calculated by $(\Delta x)^2 / \Delta t$, where Δx and Δt represent the cell length along (d) the global density gradient and the boundary layer scattering time $[(d/\delta)\tau_H]$, respectively. Here, τ_H represents the cell circulation time. Therefore, we have the following:

$$D^* \approx \frac{(\Delta x)^2}{\Delta t}. \tag{1}$$

Since particles undergo a pure random walk at the boundary layer, we can define δ as $\sqrt{D\tau_H}$. To formulate an expression for τ_H , we introduce the cellular stream function

$$\psi_0 = \sin \pi(x/d) \sin \pi \beta(y/d), \tag{2}$$

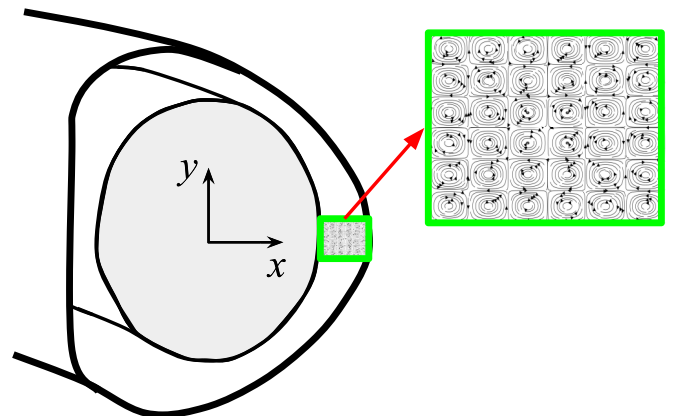


FIG. 4. Illustration of the model solved in this paper. The passive-scalar equation utilizes both Neumann and periodic boundary conditions to model the physics of core to edge in fusion devices. In our model, x and y can represent the radial and poloidal direction, respectively.

and flow velocity

$$\mathbf{u} = (\tilde{u}d/\pi)\hat{z} \times \nabla\psi, \quad (3)$$

where \tilde{u} is the maximum flow velocity. We can define the circulation time around the roll as

$$\tau_H = \frac{d}{\tilde{u}\beta}.$$

Here, the term β is the ratio of cell lengths along ($d = d_x$) and perpendicular (d_y) to the global density gradient. Plugging in these values into Eq. (1) results in

$$D^* \approx \sqrt{DD_{\text{cell}}} = D\sqrt{\text{Pe}}, \quad (4)$$

where $D_{\text{cell}} = \tilde{u}d\beta$. Here Pe represents the Peclet number,

$$\text{Pe} = \frac{\tau_D}{\tau_H}, \quad (5)$$

which is the ratio of the time for diffusion of a particle through a roll ($\tau_D = d^2/D$) to the time of circulation around the roll. Since layering in a cellular array requires that the cell circulation time be much less than the diffusion time, the result in Eq. (4) is only valid in the regime of $\text{Pe} \gg 1$. It is worth emphasizing that the effective diffusivity is not determined by simple addition as in $D^* = D + D_{\text{cell}}$, but by the geometric mean $\sqrt{DD_{\text{cell}}}$.

Many but not all properties of the nearly overlapping cells are present in magnetic confinement devices. For example, convection cells take the form of the $\mathbf{E} \times \mathbf{B}$ convection, zonal flows represent the boundary regions between cells, diffusion represents ambient collisional diffusion, and scalar concentration represents the spatial propagation of turbulent intensity. The propagation of turbulent intensity enables turbulent heat transport and thus carries a heat flux. Due to these similarities, it is convenient to review the simplest incarnation of the staircase, which is the cellular array with two disparate timescales. This model is a minimal approach to layering, which complements other ideas such as the $\mathbf{E} \times \mathbf{B}$ “predator-prey” model, where drift-wave turbulence and zonal flow populations interact via a dynamical feedback loop. Note that although this model incorporates features relevant to magnetically confined plasmas, it should not be construed as an exact representation thereof. For a brief discussion on staircases in magnetic confinement, see Appendix A.

In this paper, we explore structural fluctuations and consider the effects of an additional shear stream function on the fixed cellular array. Here, we answer the following:

- (1) Will the staircase structure form in the presence of global transverse shear and turbulence-induced mixing?
- (2) How does global transverse shear affect the mixing of scalar concentration? If we increase the strength of the shear, then what will happen to the staircase?
- (3) In a fluctuating vortex array, how does the staircase structure change? What are the criteria for a staircase to be considered resilient?
- (4) As scalar concentration flows in the fluctuating vortex array, will the staircase step or barrier develop first?
- (5) As vortices are scattered, how will the effective velocity of scalar concentration front change?
- (6) In the fluctuating vortex array, how does effective diffusivity deviate, if at all, from the $D\sqrt{\text{Pe}}$ scaling?

In the paper, we address these six questions and interpret the results in the context of magnetically confined plasmas.

B. Fixed cellular array model

The governing equation for passive-scalar transport is

$$\left(\frac{\partial}{\partial t} + \mathbf{u} \cdot \nabla\right)n = D \nabla^2 n, \quad (6)$$

where n is the scalar concentration, \mathbf{u} the fluid velocity [see Eq. (3)], and D the background diffusion coefficient. For our simulations, we set the values of \tilde{u} to 0.5. The dimensionless stream function produces the flow structure

$$\psi = \psi_0 + \alpha \psi_{\text{shear}}. \quad (7)$$

In Secs. IB and II, the value of β is set to one. In Sec. III, we calculate the average value of β by measuring the length of the cells along and perpendicular to the mean gradient. For $\alpha = 0$, the stream function creates an array of convection cells [23–25]. In section II, we explore the case of $\alpha \neq 0$. We note that Eqs. (3) and (7) follow the same normalization as the stream function and fluid velocity given in Ref. [23].

The passive-scalar equation is numerically solved on a two-dimensional grid where x and y range from $[0, L]$. The value of L and d are set to 2π and $\pi/3$ and are kept fixed for all numerical simulations and calculations performed throughout the paper. For our simulation domain, the value of d results in an array of 6×6 stationary convective cells.

We impose Neumann boundary conditions in x and periodic boundary conditions in y on the passive-scalar equation. The direction of the mean gradient is set by the Neumann boundary conditions and is similar in design to those in Ref. [26]. The Neumann boundary conditions are of the form

$$\Gamma|_{x=0} = -1 + \eta\tilde{\Gamma}, \quad (8)$$

$$\Gamma|_{x=L} = -1. \quad (9)$$

Here, $\eta\tilde{\Gamma}$ corresponds to a random scalar concentration flux, thus producing a noisy flux-driven system. The term $\eta\tilde{\Gamma}$ is also used for diagnostic purposes, such as mapping the path of the scalar concentration via a pulse train. The use of these particular boundary conditions help approximate the fixed flux condition and periodic structure found in real physical systems (e.g., magnetic confinement). An example of a physical system that demonstrates these boundary conditions is shown in Fig. 4.

To solve the passive-scalar transport equation, we use an explicit finite difference numerical scheme. The time derivative uses forward Euler and the spatial derivative uses a centered difference approach. The numerical results are accurate up to first-order in time and second-order in space.

We test the accuracy of the numerical code on the array of 6×6 stationary convective cells. The accuracy of the code is verified by producing a staircase structure and comparing the computed effective diffusivity to the validated effective diffusivity shown in Eq. (4). To determine the effective diffusivity, we drive a flux of scalar concentration at one side of the array until the staircase profile forms. We generate the staircase profile by taking an average of n along the direction

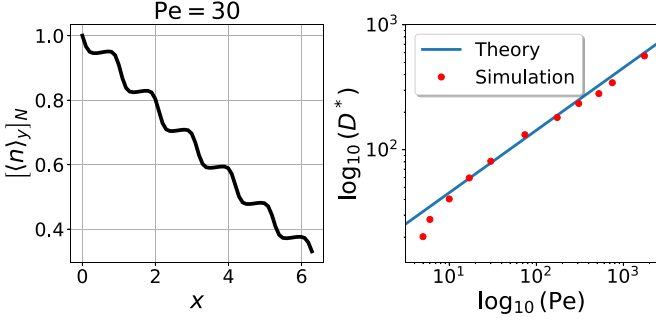


FIG. 5. Staircase profile as function of x for $Pe = 30$ and Log-Log plot of effective diffusivity D^* as a function of Pe . The validated scaling [Eq. (4)] and computational results are represented by the solid blue line and red points, respectively. Computational results follow a $1/2$ slope for large Pe number. Note that $\langle n \rangle_y$ is normalized by its max value.

perpendicular to the mean gradient

$$\langle n(x) \rangle_y = \frac{1}{L} \int_0^L n(x, y) dy. \quad (10)$$

Thereafter, we use Fick's law to calculate the effective diffusivity (D^*),

$$D^* = - \frac{(x_2 - x_1)^2}{\Delta t} \frac{n_{\text{tot}, t_f}(x = [x_1, x_2]) - n_{\text{tot}, t_i}(x = [x_1, x_2])}{\langle n_f(x_2) \rangle_y - \langle n_f(x_1) \rangle_y}. \quad (11)$$

Here x_1 and x_2 represent $(1/4)L$ and $(3/4)L$, respectively. Note that the difference between t_f and t_i is 8.3 diffusive cycles (i.e., $\Delta t = 8.3\tau_D$). For the region $[x_1, x_2]$, we define the parameter n_{tot} at a given time as

$$n_{\text{tot}} = \frac{2}{L^2} \int_{x_1}^{x_2} \int_0^L n(x, y) dy dx.$$

For a detailed explanation of how we obtain D^* , see Appendix C. We find that for a wide range of D , the staircase profile forms as long as $Pe \gg 1$. Additionally, we determine that the numerical code is sufficiently accurate and agrees with Eq. (4). A plot of $\log_{10} D^*$ versus $\log_{10} Pe$ is shown in Fig. 5 comparing both simulation and theory. Here, we demonstrate an agreement between simulation and theory for $Pe \gg 1$.

The outcome of studies regarding both transport and staircase profile resiliency to the effects of global shear and turbulence-induced variability in the flow structure are determined and discussed. The remainder of the paper is outlined here. In Sec. II, we study staircase resiliency by probing the fixed-cellular array using a global shear stream function. In Sec. III, the cellular array is relaxed by switching to a fluctuating vortex array. Here the vortex array is allowed to fluctuate by slowly increasing the Reynolds number in the Navier-Stokes equation. Finally in Secs. III A, III B, and III C, we discuss the staircase in the fluctuating vortex array, the criteria for staircase resiliency, and scalar concentration transport in the fluctuating vortex array.

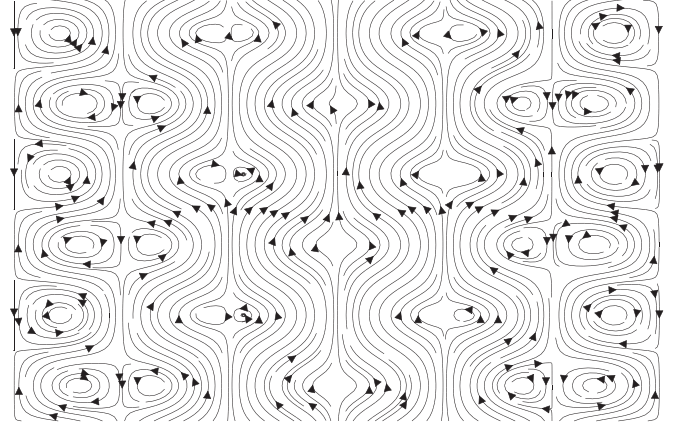


FIG. 6. Array of convective cells with parabolic shear ($m = 1$) in the y direction for the case of $\alpha = 6$. The strength of the shear in the flow is controlled by α . The increase in α , destroys the array cell structure.

II. GLOBAL SHEAR ON FIXED CELLULAR ARRAY

The effects of global velocity shear on the staircase structure are explored by including an additional shear flow,

$$\psi_{\text{shear}} = - \cos \frac{mx}{2}, \quad (12)$$

into the stream function [Eq. (7)]. As clarification, the term “shear” refers to advection in the y direction. The addition of the global shear stream function creates a new timescale, which will call the shear dispersion timescale [$\tau_{\text{adv}} = 12\pi/(\bar{u}\alpha m)$]. It is important to make the distinction that τ_{adv} represents the time for advection by ψ_{shear} across the box in y (i.e., $\tau_{\text{adv}} = L/u_S$). Note that this is different from the familiar shearing time [$\tau_S = 1/(du_S/dx)$], which is equal to $(1/3md)\tau_{\text{adv}}$.

We conduct a scan of m (i.e., the number of waves per distance L) at different integer values and different strengths, α . As a preliminary analysis, we study the physical effects that the global shear stream function has on the original cellular array flow structure. In Fig. 6, we demonstrate that increasing the amplitude of a quarter sinusoidal wave ($m = 1$) disrupts the cellular mixing structure. As stated in the introduction, cellular mixing structures are essential for the confinement of scalar concentration. Thus, it is reasonable to expect that the destruction of the cells will affect the scalar staircase profile and scalar transport.

To understand global transverse shear effects, we compare the three different timescales τ_H , τ_D , and τ_{adv} . The ratio of the diffusion timescale to the shear dispersion timescale results in

$$\frac{\tau_D}{\tau_{\text{adv}}} = \frac{\alpha \bar{m} \bar{u} d^2}{12\pi D}. \quad (13)$$

Here, we find that when the product of α and m is greater than $12\pi D/(\bar{u}d^2)$, the global transverse shear transports the passive-scalar at rate faster than diffusion. Thus, when $\alpha m > 12\pi D/(\bar{u}d^2)$, the shear dispersion time becomes an intermediate time, between τ_D and τ_H . To find the upper limit such that τ_{adv} becomes shorter than τ_H , we take the ratio of

TABLE I. Global shear timescale scenarios.

Cases	Timescales
$\alpha = 0$	$\tau_H < \tau_D$
$0 < \alpha m < 12\pi D/(\bar{u}d^2)$	$\tau_H < \tau_D < \tau_{adv}$
$12\pi D/(\bar{u}d^2) < \alpha m < 12\pi \beta/d$	$\tau_H < \tau_{adv} < \tau_D$
$12\pi \beta/d < \alpha m$	$\tau_{adv} < \tau_H < \tau_D$

the circulation timescale to the shear dispersion timescale

$$\frac{\tau_H}{\tau_{adv}} = \frac{\alpha m d}{12\pi \beta}. \quad (14)$$

Keep in mind that the value of β is set to one for this section. Here, we find that when the product of α and m is greater than $12\pi \beta/d$, the shear dispersion gives an effective mixing rate faster than inner-cell mixing. We summarize the order of the timescales in Table I.

The simulations for this section span the space of $0 < \alpha m < 45$. We cover this parameter space to capture the effects of global transverse shear on the scalar concentration staircase structure. By running simulations for different values of α and m , we can also determine the consequences that the order of time scales has on the transport of the scalar concentration.

We begin by analyzing the case of $m = 1$. For $m = 1$, we increase the value of α and study the change in $\langle n(x) \rangle_y$. We find that as the shear strength increases, the staircase profile breaks down. The staircase profile breaks down in the sense that staircase steps dissolve (see Fig. 7). As sheared flow transports the scalar concentration in the y direction, the gradient $d\langle n \rangle_y/dx$ increases in the region where global shear is dominant. Due to the nature of the shear stream function, shear is weak at the boundaries, hence the flat steps persist there [$u_S(x=0) = u_S(x=L) \sim \sin(mx/2) = 0$].

As stated in Sec. IA, the staircase structure has interspersed barriers and steps, which limit transport and trap the scalar concentration. The fast mixing in the cells trap scalar

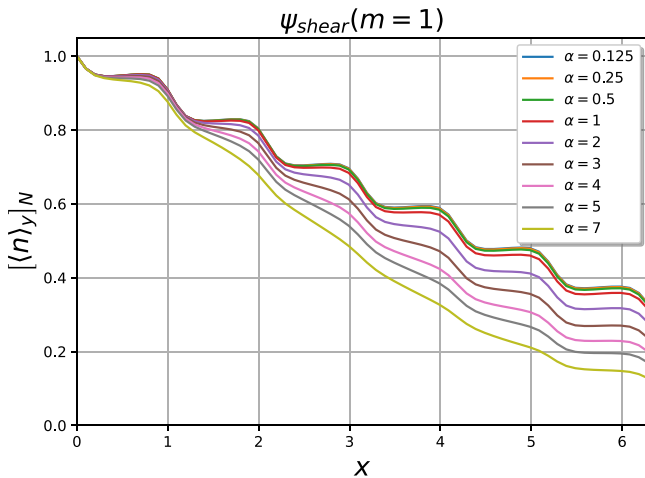


FIG. 7. Scan of normalized averaged scalar concentration in y as a function of x for $m = 1$ and different α values. As the shear strength increases, the staircase profile breaks down. Global shear flow dissolves staircase steps.

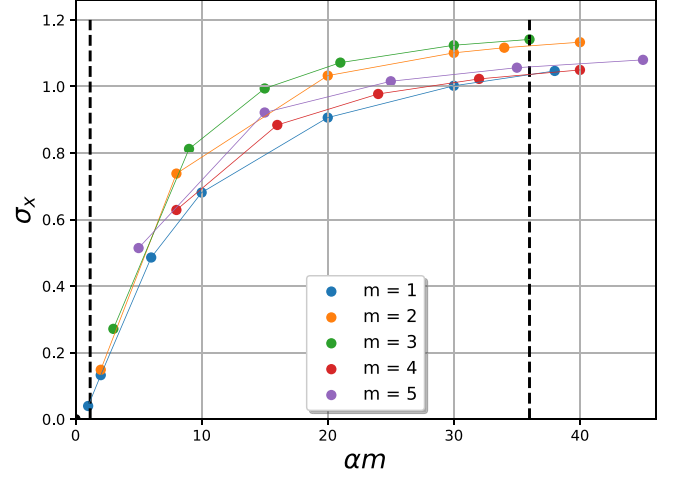


FIG. 8. Variance in x as a function of αm . For different mode numbers m , the variance grows logarithmically. We conclude that for $\alpha m > 12\pi \beta/d = 36$, the average scalar concentration profile will no longer change significantly and will be of similar form for different m .

concentration, and inter-cell barriers limit transport due to a slow diffusion time scale. By destroying the steps, the interspersed trapping of scalar concentration (due to inner-cellular mixing) no longer occurs. To understand how different values of m breakdown the staircase profile, it is convenient to assess the deviation of the $\langle n \rangle_y$ profile from the original staircase profile ($\alpha = 0$). By doing so, we can also measure the total scalar concentration in the flow as a function of staircase profile deviation.

To quantify, for different m , the deviation or breakdown of the staircase profile, the variance with respect to x is calculated for different α values,

$$\sigma_x^2 = \int_0^L (\langle n \rangle_y - \langle n_0 \rangle_y)^2 dx. \quad (15)$$

Here, we define the baseline staircase profile ($\alpha = 0$) as $\langle n_0 \rangle_y$. The variance measures the deviation between the $\alpha \neq 0$ profiles and the baseline staircase. In Fig. 8, we plot the square-root of Eq. (15) as a function of αm . In the plot, we mark the transition points where the different order in time scales occur [$\alpha m = 12\pi D/(\bar{u}d^2)$ and $\alpha m = 12\pi \beta/d$] as black dashed vertical lines. The graph shows a similar trend in the variance for distinct mode numbers (m). For each mode number, the increase in α results in a significant increase in the deviation up to values of $\alpha m \sim 12\pi \beta/d$. For values of $\alpha m > 12\pi \beta/d$, the variance plateaus at $\sigma_x \sim 1.19$ for all m . The plot of the variance shows that up to a critical shear of $\alpha m = 12\pi \beta/d$, the $\langle n \rangle_y$ profile for different mode numbers will be similar in form and no longer notably change throughout the regime of $\tau_{adv} < \tau_H < \tau_D$. To summarize, we show that the $\langle n \rangle_y$ profile deviates significantly in the regime of $\tau_H < \tau_{adv} < \tau_D$, but goes unchanged once $\alpha m > 12\pi \beta/d$.

Next, we want to explore how the order in timescales affects the dynamics of the scalar concentration transport. In Fig. 7, we observe that as α increases, the staircase steps gradually dissolve, resulting in an increase in $d\langle n \rangle_y/dx$. Thus, the scalar concentration is no longer trapped by the cells, as

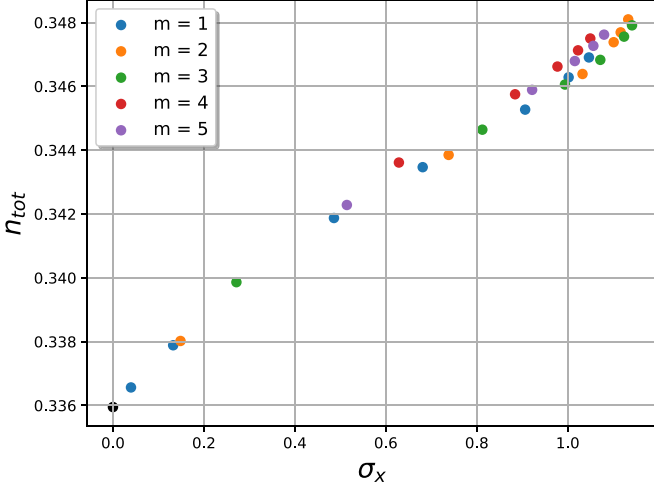


FIG. 9. Total scalar concentration as a function of the variance in x . The total scalar concentration increases as the scalar concentration profile deviates from the staircase ($\alpha = 0$) profile. Global shear weakens mixing in the x direction. The value of $d\langle n \rangle_y/dx$ increases with shear, thus improving confinement of scalar concentration.

advection in the y direction becomes the dominant form of transport. With increasing $d\langle n \rangle_y/dx$, the transport (in x) due to cell circulation is reduced. To assess whether shear diminishes mixing along x and its relation to the deviation of the staircase profile, we calculate the total scalar concentration for various values of m and α ,

$$n_{\text{tot}} = \frac{1}{L^2} \int_0^L \int_0^L n(x, y) dy dx. \quad (16)$$

In Fig. 9, we show a line with positive slope between the total scalar concentration and σ_x . We find that as the pattern of staircase corrugation decays, the total scalar concentration increases. Hence, the increase in global shear weakens/strengthens the mixing of scalar concentration along/perpendicular to the mean gradient. We note that as σ_x approaches 1.19, the total scalar concentration does not change significantly. Thus, transport of scalar concentration can no longer be suppressed once it surpasses a value of $\alpha m = 12\pi\beta/d$. Nevertheless, results show that an additional global sinusoidal shear flow *weakens* the staircase structure and reduces the transport of scalar concentration in x for values of $\alpha m > 12\pi D/(\bar{u}d^2)$.

The question of whether Eq. (4) can help explain the suppression of scalar concentration may arise. The answer to this question is no. With increasing shear strength (α), the global shear disrupts cellular mixing structures, causing scalar concentration to advect in the y direction. In this context, explaining the suppression of scalar concentration cannot be achieved via Eq. (4). This is due to the condition that requires cell boundaries to be intact.

In the next section, the cellular array will be allowed to relax and fluctuate. There, we will discuss the effects that the relaxed vortex array has on the staircase robustness and scalar transport.

III. RELAXATION IN A FLUCTUATING VORTEX ARRAY

Up till now, the research presented in this paper has involved only a slight modification to the problem of the fixed cellular array studied in Ref. [23]. We argue that the fixed cellular array setup is contrived and overly constrained; therefore, it is an unrealistic representation of physical systems observed in nature. Such physical systems will manifest variability, fluctuations, and intrinsic jitter. Thus, the cell pattern is more like a *melting vortex array* than a frozen array. Hence, we study the dynamics of a less constrained cell array (i.e., vortex array with fluctuations) and ask how resilient the staircase profile is in the presence of fluctuations. In addition to that, we give answers to the following:

(1) What happens to interspersed regions of strong scalar concentration mixing as cells relax? What about other cellular interactions?

(2) What is the behavior of the scalar concentration trajectory through the vortex array? As we increase fluctuations in the vortex array, how will the speed and trajectory of the scalar concentration front change (see Fig. 24)?

(3) How does the increase in scattering in the vortex array affect the transport of scalar concentration?

To answer these questions, we use the model of a “melting vortex crystal,” advanced in Refs. [27,28]. In this setup, a spatially periodic force creates the vortex array pattern. The vortex array flow is driven and damped by both viscosity and drag. The fluctuations of the vortex array can be explored systematically by scans of modest Reynolds numbers. Here, the Reynolds number is set by the forcing strength. Such a variable vortex array flow is akin to a melting crystal, where “melting” is related to the turbulent mixing field. By systematically varying the vortex array state (i.e., the degree of melting), one can explore the connection between cell size perturbations and staircase-variability.

The governing equation for the vortex array is the 2D Navier-Stokes (NS) equation, which can be written in nondimensional form as

$$\left(\frac{\partial}{\partial t} + \mathbf{u}_{fv} \cdot \nabla \right) \omega = \frac{1}{\Omega} \nabla^2 \omega + F_\omega - \alpha \omega, \quad (17)$$

$$\nabla^2 \psi_{fv} = \omega. \quad (18)$$

We write the 2D incompressible NS equation in terms of the stream function ψ_{fv} and vorticity $\omega = \nabla \times \mathbf{u}_{fv}$, where $\mathbf{u}_{fv} = \hat{z} \times \nabla \psi_{fv}$ is the fluid velocity at position \mathbf{x} and time t . Note that \mathbf{u}_{fv} is not the same flow velocity [Eq. (3)] we insert into the passive-scalar transport equation [Eq. (6)]. For a derivation of Eq. (17) and control parameters, see Appendix B. The spatially periodic force F_ω in the NS equation is defined as

$$F_\omega \equiv -n^3 [\cos nx + \cos ny]/\Omega. \quad (19)$$

Here n represents the injection wave vector and is set to $n = 4$ for all simulations. The boundary conditions for Eq. (17) are periodic in both x and y direction. In Eq. (17), there are two control parameters: the nondimensional Ekman-friction α and Ω . Here, Ω is equivalent to the familiar and intuitive Reynolds number. Note that the velocity is set by the forcing. We can define Ω as the ratio of the viscous timescale ($\tau_v = \nu^2/k^2$) to the cell circulation timescale ($\tau_H = nk\nu/F_{\text{amp}}$). The alpha parameter is defined as the ratio of cell circulation timescale

to the mean shearing timescale ($\tau_S = 1/\alpha'$). Thus, the two control parameters are

$$\Omega = \frac{\tau_v}{\tau_H}, \quad (20)$$

$$\alpha = \frac{\tau_H}{\tau_S}. \quad (21)$$

Here F_{amp} is the forcing amplitude, k inverse length scale, ν the kinematic viscosity, and α' the dimensional Ekman friction. The value of α affects large-scale flow and Ω affects small scale flow and also the strength of the forcing function, F_ω . In this setup, the spatially periodic force F_ω yields, at $\Omega < 5.5$, a zero fluctuating vortex array.

The NS equation is solved numerically by using a pseudo-spectral method with 2/3 dealiasing cutoff and the fourth-order Runge-Kutta method for the time steps. The time step used here is $\delta t = 0.01$ with a spacial grid set to $N = 128$. To make sure that the temporal evolution of the system is obtained accurately, typical runs consist of 3×10^6 time steps. We remind the reader that this numerical scheme differs from that used to solve Eq. (6). Here, we employ the same numerical methods as Refs. [27,28], aiming to replicate the results obtained in those works. By employing this numerical scheme, we can precisely generate, classify, and validate various stages in the evolution of the fluctuating vortex array.

Before discussing the destabilization of the zero-temperature vortex array state, the initial vorticity in the DNS has the form

$$\omega = \omega_s + 10^{-4} \sum_{m_1=1, m_2=1}^{2,2} [\sin(m_1 x + m_2 y) + \cos(m_1 x + m_2 y)] m_2^2 / \sqrt{m_1^2 + m_2^2},$$

where $\omega_s = -n[\cos(nx) + \cos(ny)]$. The system is evolved by the application of the force F_ω . Here, exploration of the different fluctuating vortex array stages is done by slowly increasing the value of Ω . Note that this study focuses on low-modest Reynolds numbers ($\Omega = 4\text{--}40$), mainly exploring a regime of spatiotemporal chaos. The fluctuating vortex array model allows us to realize similar physics to that which occurs in actual physical systems (e.g., drift-wave turbulence). For all simulations, the following are output (a) the total kinetic energy $E(t) \equiv \bar{\mathbf{u}}_{fv}^2$ and (b) the stream function ψ_{fv} .

We use the value of Ω to categorize the different stages in the evolution of the fluctuating vortex array. We denote the onset of cellular fluctuations as Ω_s . Here Ω_s is the effective Reynolds number where cellular fluctuations occur. When $\Omega < \Omega_s = 6$, the vortex array is referred to as a zero-temperature vortex array. The vortex array is allowed to fluctuate by increasing Ω from the stable state Ω_s , in increments of 0.5. This allows us to clearly mark transitions between states of the flow in the vortex array. The transitions are marked as follows: SX, the zero-temperature vortex array imposed by the force; followed by SXA, steady distorted array; leading to a distorted array that oscillates in time, either periodically (OPXA) or quasiperiodically (OQPXA); last, the system becomes disordered and exhibits spatiotemporal chaos and turbulence (SCT). Here spatiotemporal chaos means that the temporal evolution of the system becomes disorder and

TABLE II. Different stages of the fluctuating vortex array. In this paper we consider small and large Ω any value within SX and SCT range, respectively.

Transitions	Ω Range
SX	$\Omega < 6$
SXA	$6 < \Omega < 7$
OPXA/OQPXA	$7 < \Omega < 13$
SCT	$13 < \Omega$

the spatial organization of the vortex array is distorted (i.e., flow patterns appear and disappear in irregular fashion). A table of these transitions is provided in Table II. In Fig. 10, we show the energy time-trace for each of these transitions. These stages are categorized based on the behavior of the energy time-trace and its autocorrelation. In the autocorrelation analysis of the energy, we measure the relationship of the observations between the different points in time, and thus seek a pattern or trend in the time series. For states of SX and SXA ($\Omega < 7$), the energy autocorrelation is 1 for all lags, while for OPXA and OQPXA ($7 < \Omega < 13$), the energy autocorrelation oscillates with the frequency of the periodic fluctuation for lag greater than zero. In the case of the chaotic/turbulent state ($\Omega > 13$), the energy autocorrelation value is low (~ 0) for all lags.

Before injecting the passive scalar into the flow, we address the question of ‘‘cellular interactions’’ as the cells are allowed to relax. This discussion will be of use when later discussing the staircase structure and transport of scalar concentration in the vortex array. It’s important to note that the flow will evolve differently depending on the values chosen for k , ν , and α' . For our study, we assign the following values to each parameter: $k = 10$, $\nu = 10^{-2}$, and $\alpha' = 0.55$. To understand the consequence of this, we have to look at the timescale definition of the control parameters $\Omega = \tau_v/\tau_H$ and $\alpha = \tau_H/\tau_S$. At this point, the alert reader will notice that the amplitude of the forcing (F_{amp}) couples α and Ω . Therefore, the two values are inversely proportional to each other. It is clear from Fig. 11 that $\Omega\alpha > 1$ for all simulations. In timescale notation, this means that $\tau_S < \tau_v$, which implies that large-scale flows

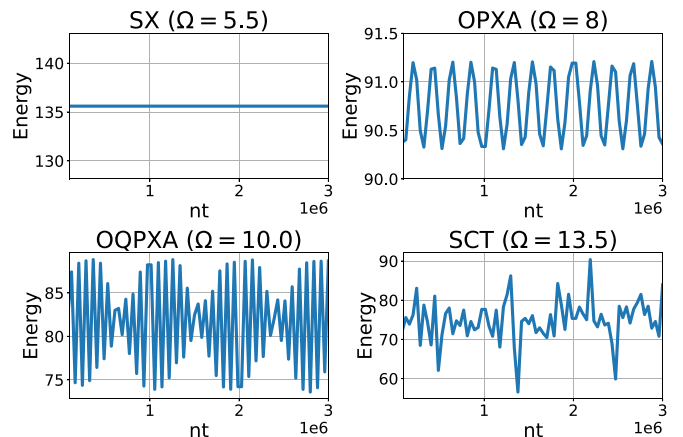


FIG. 10. Energy time-trace for the different stages of the fluctuating vortex array. Here nt represents the time-steps in the DNS.

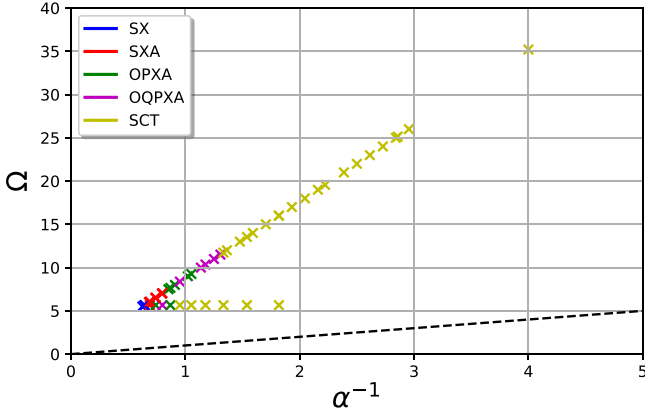


FIG. 11. Plot of simulations in Reynolds (Ω) and $1/\alpha$ number space. Here Ω and $1/\alpha$ control turbulent mixing and large-scale flows. The different stages of the fluctuating vortex array are highlighted in different colors. All simulations ran in this study fall in the regime of $\tau_v > \tau_s$.

develop at a rate faster than fluid momentum diffuses over a scale length (n/k). Here, the diffusion of the fluid momentum is associated with the excursion of a cell during cell array fluctuations.

As a consequence of the $\tau_s < \tau_v$ condition, as Ω increases, cells merge. An increase in Ω , such that $\Omega > \Omega_s$, perturbs the location of the cells. This perturbation causes cells to run into each other and merge (see Fig. 12). The merging of flow lines results in vortices merging and forming larger vortex structures, which over time, develop into large-scale flows. We confirm this by qualitatively studying the contour plots of the stream function at different stages of the fluctuating vortex array (see Fig. 13). In addition to this, we observe that only vortices of the same sign merge.

To quantitatively analyze the formation of large-scale flows, we investigate the influence of the nondimensional Ekman-friction parameter (α) on the fluctuating vortex array. In Fig. 14, we present an investigation of the α parameter. The solid blue line in the graph depicts the energy of the zero-temperature vortex array in wave number (k) space. When α is sufficiently large (~ 1.6), the parameter dampens both large

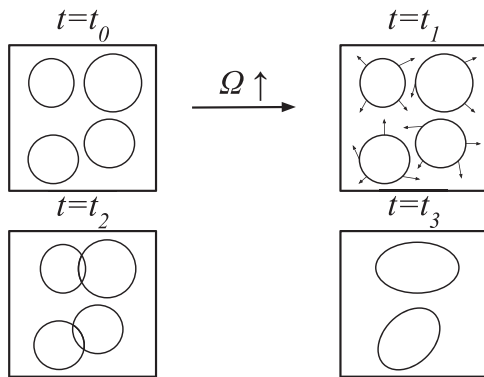


FIG. 12. An increase in Ω , such that $\Omega > \Omega_s$, perturbs the location of the cell. Cells then run into each other and merge. Here, Ω_s represents the onset of cellular fluctuations.

and small scale flows. For large α , the flow follows the frozen vortex array pattern dictated by the external force F_ω . Here, energy is concentrated at the wave injection number $k = 4$. While maintaining a constant Ω ($\Omega \sim 5.7$), we decrease the value of α . The graph's dashed red line illustrates the evolution of the energy as α transitions to a lower value. At a lower value of α , the energy increases significantly for values of k less than 4. This demonstrates that small values of α imply large-scale flow structures (where the value of α serves as a control for large-scale flows).

As an extension to the previous assessment, we use the Okubo-Weiss field to measure the evolution of large-scale flows relative to vortices as the value of Ω increases. The Okubo-Weiss field (Λ) is defined as

$$\Lambda = \frac{\partial u_x}{\partial x} \frac{\partial u_y}{\partial y} - \frac{\partial u_x}{\partial y} \frac{\partial u_y}{\partial x}. \quad (22)$$

The Okubo-Weiss field gives the difference between square vorticity and square shear strain [29,30]. The quantity Λ characterizes the local topology (i.e., Gaussian curvature of streamlines) of an incompressible two-dimensional fluid flow. Here, Λ is a distinctive measure of fluid properties, particularly in distinguishing and describing regions dominated by deformation and rotation. In Fig. 15, we plot the ratio of $\Lambda < 0$ to $\Lambda > 0$, which corresponds to the ratio of the area of saddles to the area occupied by centers, respectively. The increase in Ω results in an increase in the population of saddles relative to centers, which coincides with our previous assessment based on the evolution of energy in wave number space.

For different stages of the fluctuating vortex array, the stream function (ψ_{fv}) is output from the vorticity equation [Eq. (17)]. It is important to note that $(\nabla \psi_{fv})_{fv}$ is dimensionless, thus when inserting into Eq. (3) we make the following transformation, $\nabla \psi = (\pi/d)(\nabla \psi_{fv})_{fv}$. We insert this into the passive-scalar equation [Eq. (6)] through the velocity term [Eq. (3)],

$$\mathbf{u} = (\bar{u}d/\pi)\hat{z} \times \nabla \psi = \bar{u}(\hat{z} \times (\nabla \psi)_{fv}). \quad (23)$$

By doing this normalization, we can compare passive scalar transport in the fluctuating vortex array to the fixed cellular array. The scalar concentration is evolved in this flow using the same boundary conditions discussed in Sec. IB. In the following subsections, we present the effects large-scale flows and vortex fluctuations (in the regime of $\tau_v > \tau_s$) have on staircase structure resiliency and passive-scalar transport.

A. Staircase profile in the vortex array

Now that we have a general understanding of how Ω affects cellular interactions and flow dynamics, we drive a flux of scalar concentration (similar to Sec. IB) in the flow created by Eq. (23). We stress that simply using Eq. (10) will not result in a staircase profile. Here, the average of the scalar concentration must be calculated at different orientations to recover the staircase profile. By doing so, we can establish a connection with the fixed cellular array (i.e., baseline case) and show that oblique staircases exist, which can influence transport in x .

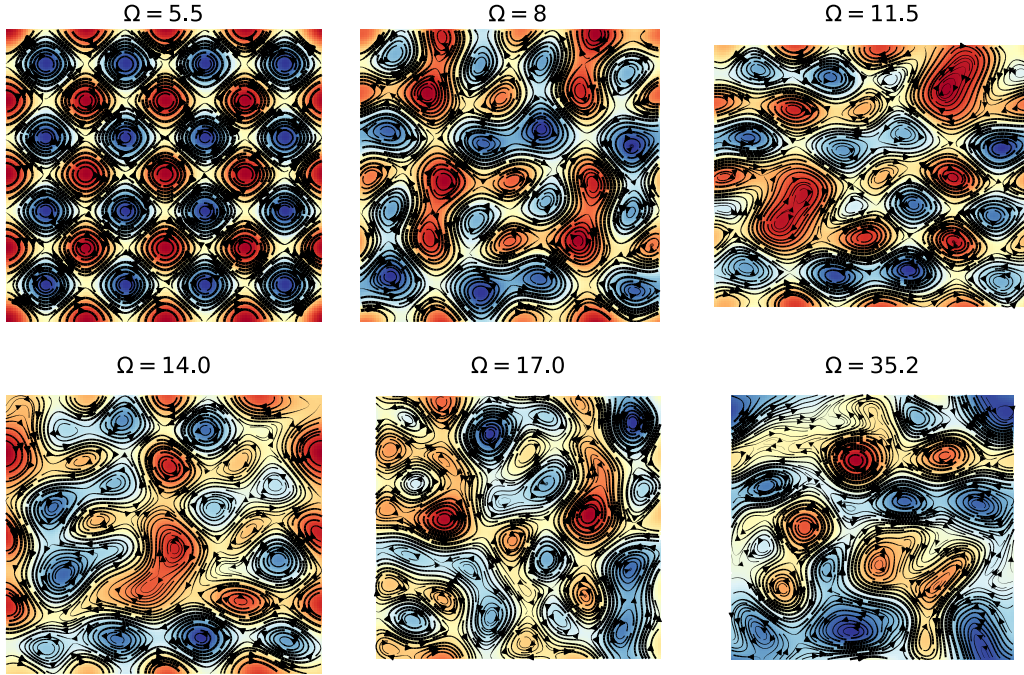


FIG. 13. Contour plots, illustrating different stages of the fluctuating vortex array. As Ω increases, there is a merger of vortices along with distortions of the cellular flow array. Growth in Ω leads to scattered vortices and large-scale flow structures.

To produce the staircase profile, we rotate the scalar concentration field in two different directions, $\theta = \pm\pi/4$, with respect to x . In Fig. 16, we illustrate the averaging along one of the orientations. Therefore, we now define the average of the scalar concentration as

$$h(x') = \langle n(x') \rangle_y = \frac{1}{L'} \int_0^{L'} n(x', y') dy'. \quad (24)$$

Here, the terms x' and y' represent the x axis and y axis in the two different orientations. In terms of L , the value

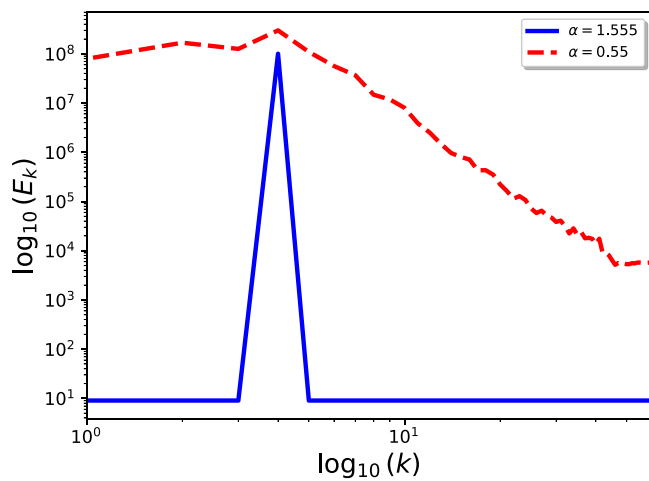


FIG. 14. Log-log plot of the energy as a function of the wave number k for different α . The decrease in the α parameter results in large-scale flows. The solid blue line denotes the zero temperature cellular flow ($\Omega \sim 5.7$), where all energy is mainly focused on $k = 4$. As α decreases, the energy grows for smaller k , as shown in the dashed red line.

of L' is $0.82L$. To setup a baseline case, we consider the zero-temperature vortex array. In this stage, the average scalar concentration profile (Fig. 17) takes the form of the staircase presented in Ref. [23]. We note that for the case of $\Omega = 0$ (i.e., no fluctuations), the result is the same since the vortices become locked in the cellular array pattern.

We repeat the same process for different stages of the fluctuating vortex array. As cells are scattered from the zero-temperature state, the cells begin to merge, resulting in larger cell structures. The formation of large cell structures is a consequence of the $\tau_S < \tau_V$ condition, which we discuss in detail in Sec. III. In Fig. 18, we examine two different cases, namely $\Omega = 8$ and $\Omega = 11.5$. Here, the two contour plots of the scalar concentration demonstrate that cell streamlines connect for several cell structures. The connection of cell

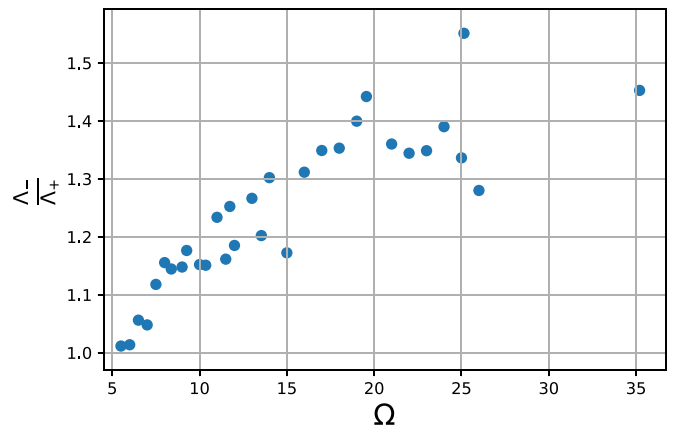


FIG. 15. Plot of saddle area (Λ_-) to center area (Λ_+) as a function of Ω . In the regime of $\tau_V > \tau_S$, fluctuations lead to large-scale flows, thus the area of saddles increase compared to area of centers.

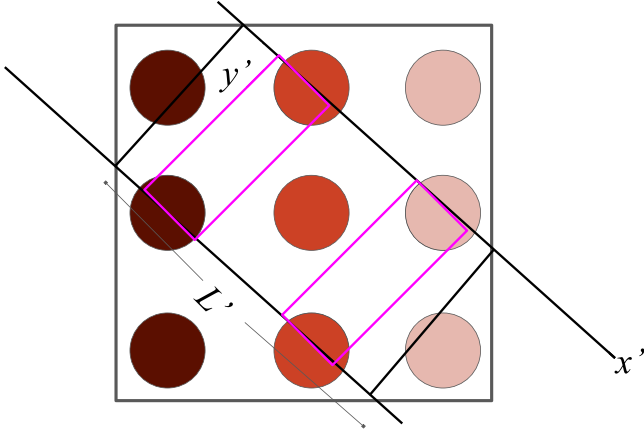


FIG. 16. Illustration of the incline scalar concentration averaging. We note that averaging along y' as a function of x' leaves out cells due to y' and x' cutoffs. The cutoffs will make it appear as if $\langle n \rangle$ leaves steps.

streamlines reflect as mergers in staircase steps in the average scalar concentration profile. By looking at the profile of h , one can mistakenly interpret that there are no steps or that steps are missing. To explain this, we emphasize that steps become elongated due to vortex mergers and that the missing steps correspond to the cutoffs of the incline scalar concentration averaging, as shown in Fig. 16. The rest of the fluctuating vortex array stages are summarized through analysis of the step-size (Fig. 19) and curvature of the staircase profile (Fig. 20) as a function of Ω .

To assess the mergers in steps, we measure the step length at different values of Ω (see Figs. 18, 19, and 21, 22). Here, the average and maximum step length in the staircase structure grows with Ω . This analysis verifies that cell mergers result in elongated staircase steps (as discussed in Fig. 18). The plot of the step-size also confirms that as Ω increases, the cells in the flow grow in size.

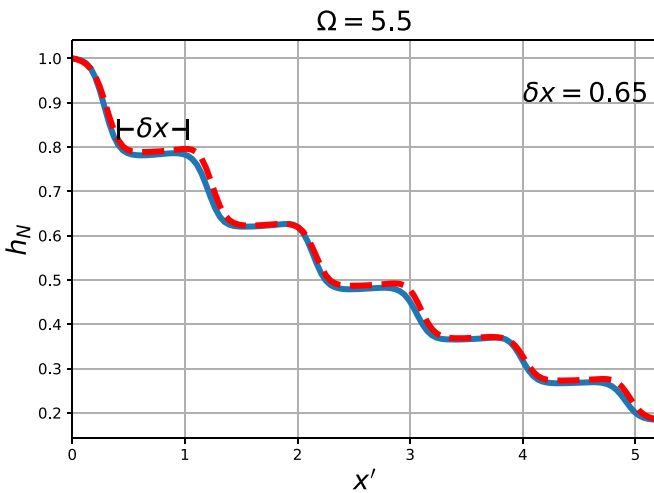


FIG. 17. Illustration of the zero temperature cellular flow structure. The solid blue and dashed red plot lines correspond to averaging in the $\theta = -\pi/4$ and $\pi/4$ direction. In the zero temperature vortex array, the staircase profile for the blue (solid) and red (dashed) normalized $h(x')$ plot lines are the same.

In addition to step measurements, we calculate the curvature of the scalar concentration profile. Based on our study of Figs. 19 and 18, as the vortex array relaxes, the number of steps decrease due to mergers. The result of step mergers means there are fewer interspersed regions of corrugations. To measure the interspersed regions of corrugations, we calculate the curvature of the scalar concentration profile

$$\kappa = \int_0^L \frac{h''(x')}{(1 + h'(x')^2)^{3/2}} dx', \quad (25)$$

where $h(x')$ represents Eq. (24). We discern in Fig. 20 that the increase in Ω results in the decrease of κ . It is important to note that the value of κ does not vanish, but instead remains above ~ 1.5 for large values of Ω . Here, κ quantifies and describes the step length scale in the staircase. Large and small values of curvature represent small steps and big steps, respectively. Similarly, the value of κ can also be interpreted as a measure of the number of steps or interspersed regions of corrugations in the staircase profile. Hence, the profile curvature is a signature of layering.

B. Staircase resiliency

In this subsection, we provide an in-depth discussion on staircase resiliency. So far, we have only provided evidence that staircase structures persist up to modest values of Reynolds numbers. To give a precise meaning to the statement of “resiliency,” a set of criteria must be established.

First and foremost, $Pe \gg 1$ is a necessary condition for the formation of transport barriers in the process of scalar mixing, as mentioned in Sec. IA. Maintaining $Pe \gg 1$ over a relevant range of Reynolds numbers is thus one natural criterion for “resilience.” It is of use then to calculate Pe for different stages of the fluctuating vortex array. Since we control the max flow velocity and background diffusivity ($D = 1.7 \times 10^{-2}$), the Pe number only depends on the dimensions d_x and d_y of the cells. As discussed in Sec. IB, d represents the length of the cell in the direction of the mean gradient (d_x) and β represents the ratio of d_x to the length of the cell perpendicular to the mean gradient (d_y). By using the stream function (ψ_{fv}), we can determine the average size of the cells in the flow to calculate the Pe number. In Fig. 23, we show for values of Ω greater than 25 that Pe decreases up to a value of ~ 17.5 . Hence, the $Pe \gg 1$ criterion is satisfied for the range of $0 < \Omega < 40$.

On the topic of Pe , it is useful to measure the ratio of Pe to Reynolds numbers used here. We can define the Schmidt number, which measures the ratio of momentum diffusivity to scalar diffusivity,

$$Sc = \frac{\tau_D}{\tau_v}. \quad (26)$$

For our simulations, we operate in a regime of $Sc = [0.5, 7.5]$. It is unclear whether maintaining $Sc \sim \mathcal{O}(1)$ is a strict or necessary requirement to sustain the staircase structure. In future work, we plan to study the Sc number in more detail.

A second criterion is that a staircase should maintain a sufficiently high curvature (equivalent to sustaining a sufficient number of steps) over the relevant range of Ω values. The precise critical value of curvature (κ) is not determined, though our studies suggest $\kappa \gtrsim 1.5$ is an adequate value for

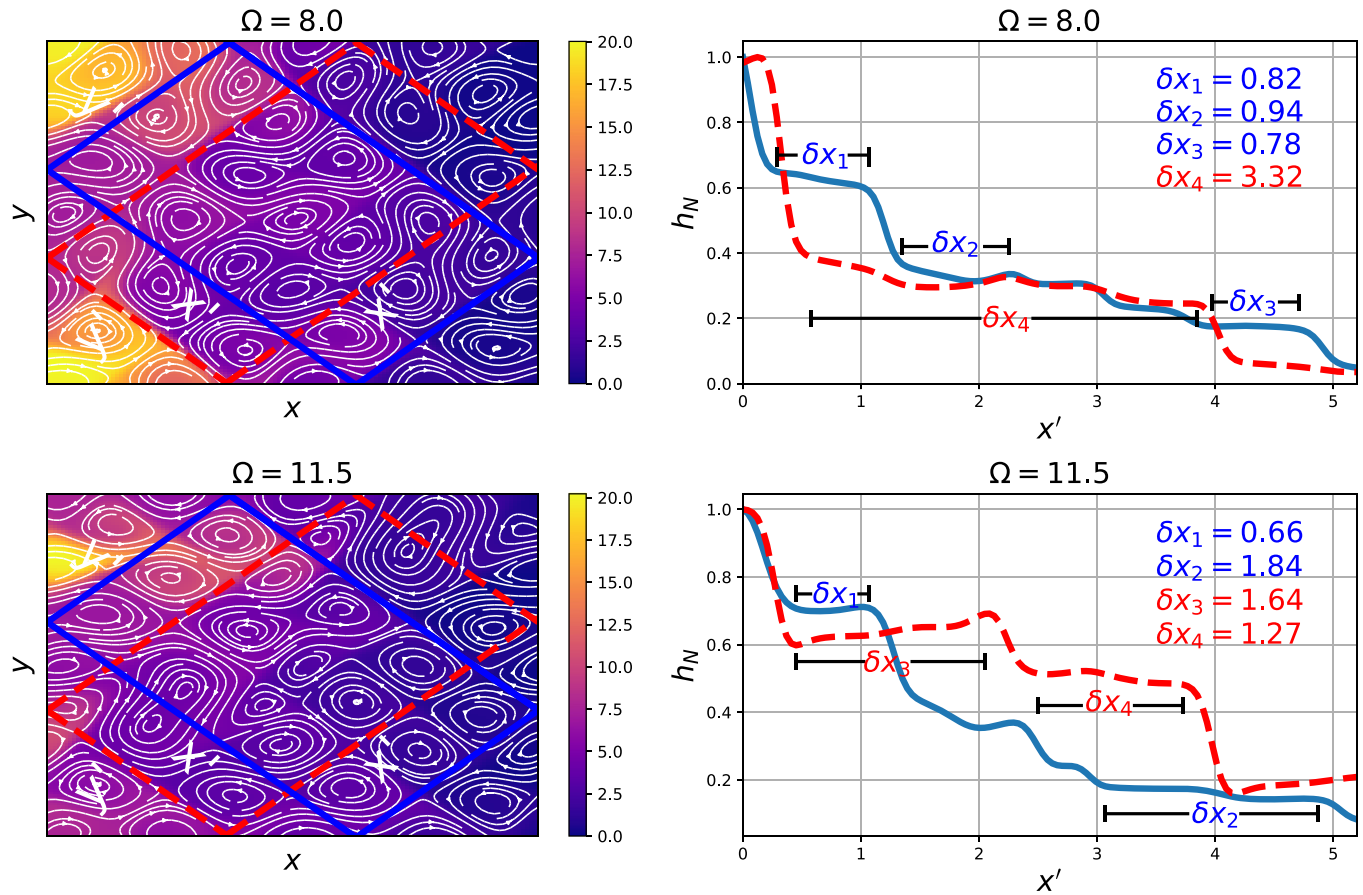


FIG. 18. Snapshot of passive-scalar concentration for the case of $\Omega = 8.0$ and $\Omega = 11.5$. On the left figures, the streamlines display mergers/connections of vortices. These mergers are reflected on the normalized $h(x')$ profiles on the right, by the elongated staircase step on the solid blue and dashed red line. The blue (solid) and red (dashed) plot lines correspond to averaging in the $\theta = -\pi/4$ and $\theta = \pi/4$ directions with respect to x . As the cells fluctuate from the zero temperature state, the staircase structure remains robust. We indicate steps as regions where $dh/dx' \sim 0$. These are clearly separated by distinct jumps (i.e., regions of corrugations).

a staircase. In Fig. 20, the plot of κ versus Ω shows that κ is greater than 1.5 for most values of Reynolds numbers. Even for the largest Reynolds number studied, κ does not

vanish, though it does decrease as the staircase coarsens due to mergers. To substantiate this assertion, we present Figs. 21 and 22, which illustrate the presence of staircase structures

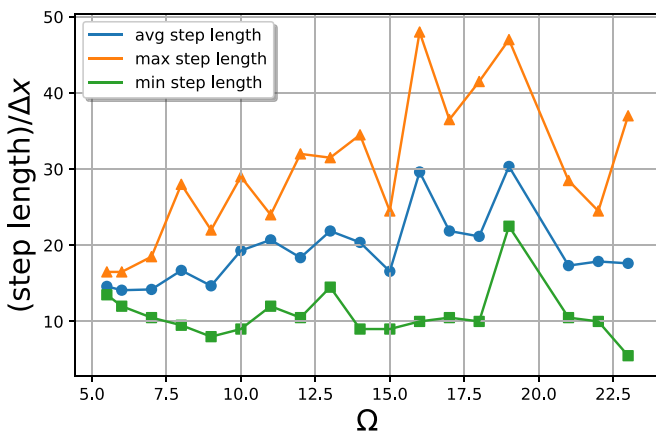


FIG. 19. Plot of step size divided by the spatial grid spacing ($\Delta x = L/N$) as a function of Ω . As the vortex array fluctuates, cells begin to merge, leading to overall average step size and max step size increase.

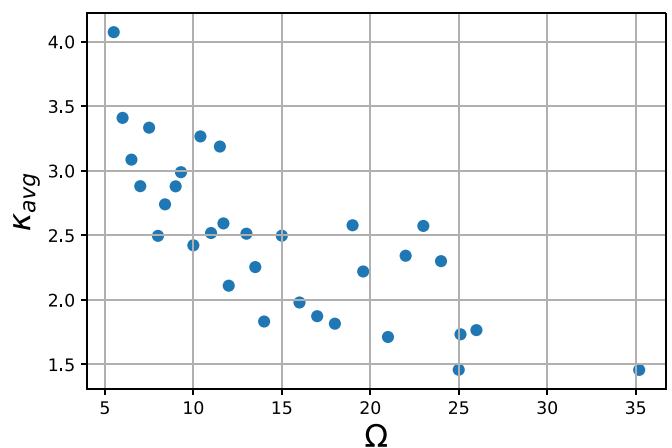


FIG. 20. The plot of the curvature as a function of Ω . As cells scatter, the merger of steps decrease interspersed regions of corrugation, hence a decline in $h(x')$ curvature.

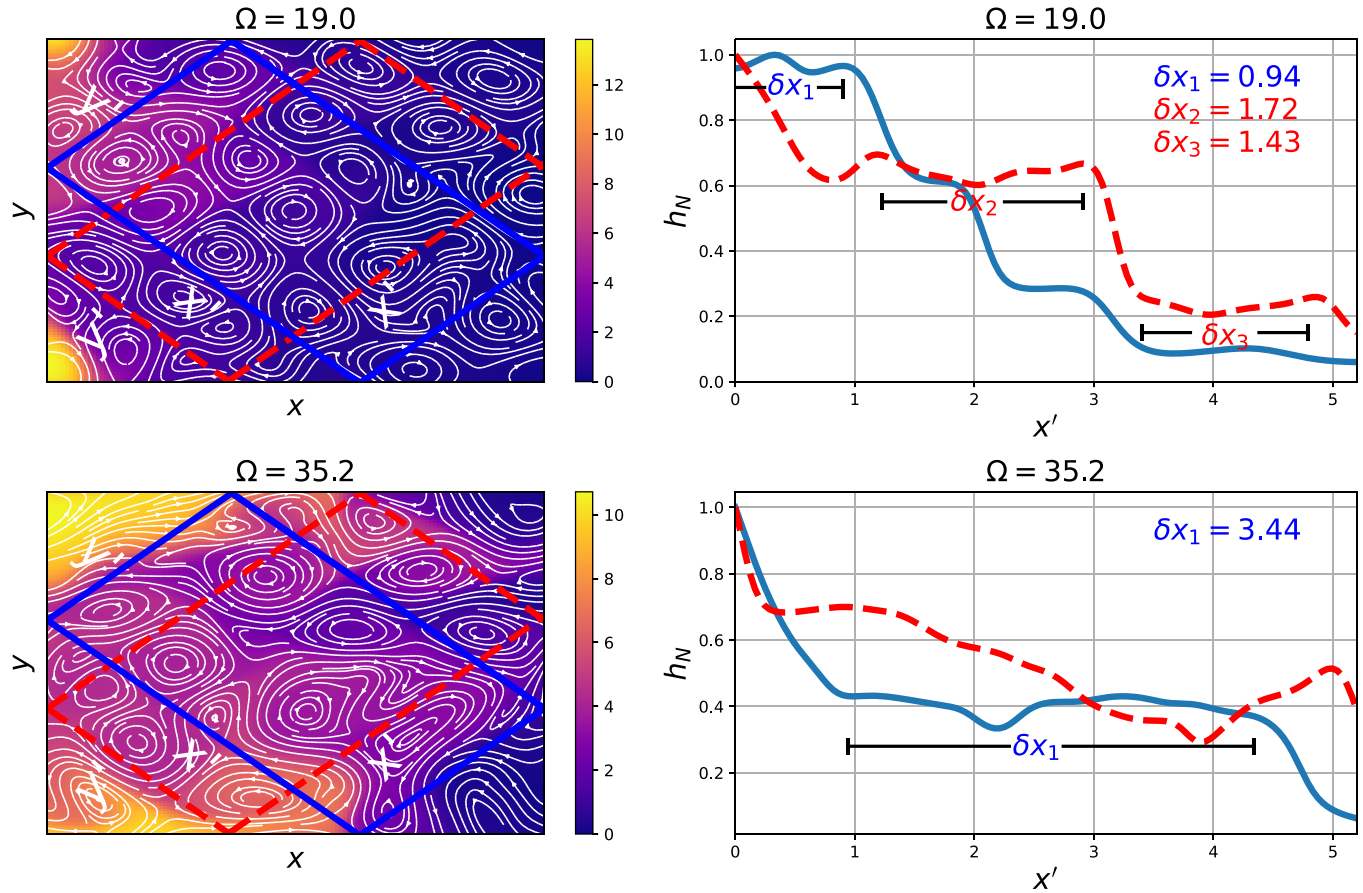


FIG. 21. Snapshot of passive-scalar concentration for the case of $\Omega = 19.0$ and $\Omega = 35.2$. Similar to Fig. 18, cell mergers are reflected on the normalized $h(x')$ profiles on the right. Here, we demonstrate evidence that the staircase structure persists up to the value of $\Omega = 35.2$.

at the highest values of Ω . Hence, we identify the condition $\kappa \geq 1.5$ as a second criterion.

Therefore, resilience of a staircase over a given range of Ω requires:

- (1) $Pe \gg 1$, so barriers are formed and maintained.
- (2) $\kappa \geq 1.5$, so a requisite number of steps is sustained.

Clearly, criterion (1) is based on first principles, while criterion (2) is empirical, and emerges from our studies. Finally, we speculate that the curvature criterion (2) may be ultimately related to the $Pe \gg 1$ criterion (1). However, we are unable to report anything further at this time. We summarize the criterion for resiliency discussed here in Table III. In the following subsection, we will direct our attention to the transport of the scalar concentration in the vortex array.

C. Transport in the vortex array

In this subsection, we explore the trajectory and transport of scalar concentration in the vortex array. Note that the scalar

concentration trajectory is the path that an element of scalar concentration (i.e., scalar particle) takes to reach the right boundary (see Fig. 24). In the process of scalar concentration reaching the right boundary it's of use to understand how interspersed regions of corrugations form (i.e., how a staircase structure forms).

We find that in the process of forming a staircase, the scalar concentration forms a “web” structure. The web structure represents the flow of scalar concentration along regions of strong shear and around vortices. In Fig. 25, we see that barriers in the staircase form before steps because scalar concentration travels *along* cell boundaries first. Based on previous examination of the Okubo-Weiss field (see Fig. 15), the increase in Ω will result in a wider scalar concentration path (i.e., the web will form thicker fibers). To understand how the widening of the scalar concentration path affects the scalar trajectory, we apply a pulse train of scalar concentration to the left boundary [Eq. (11)].

When scalar concentration is injected into the flow via a pulse train method, a flamelet network pattern forms (see Figs. 26 and 27). As stated in Ref. [31], flamelet fronts are visible in the regime of Peclet and Damköhler (Da) numbers much greater than one. The nondimensional number Da is defined as the ratio of cell circulation to reaction time. Here, the reaction time corresponds to the speed of the scalar concentration front propagation, which is faster than the cell rotation speed. We define “front” as the scalar concentration’s

TABLE III. Criterion of staircase resiliency.

Staircase Resiliency Criterion	
Peclet number	$Pe \gg 1$
Curvature	$\kappa \geq 1.5$

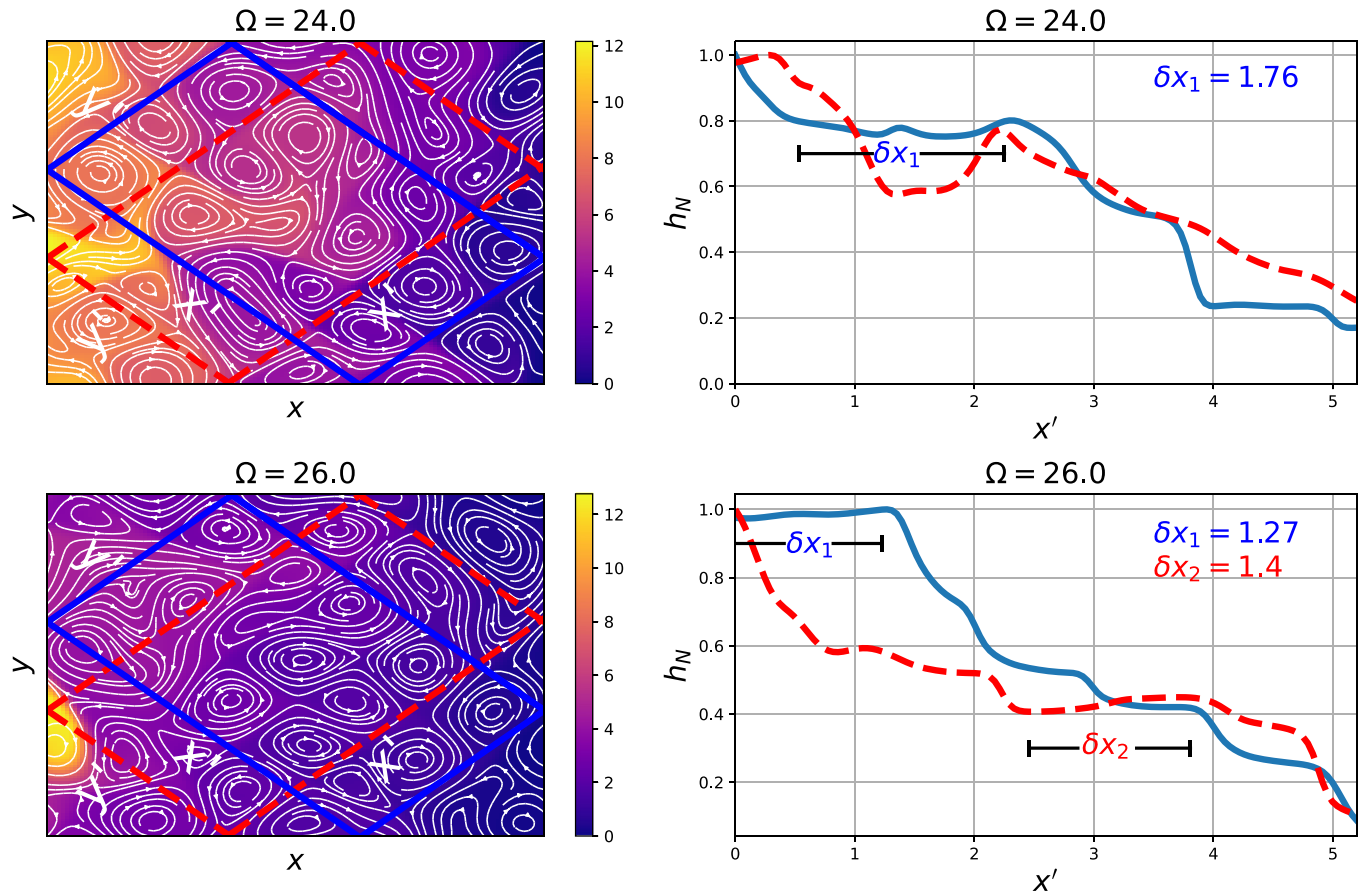


FIG. 22. Snapshot of passive-scalar concentration for the case of $\Omega = 24.0$ and $\Omega = 26.0$. Similar to Fig. 21, we demonstrate the persistence of the staircase structure for $\Omega < 40$.

furthermost point in x . The regime of $Pe \gg 1$ and $Da \gg 1$ is also known as the weak advection regime [32–36]. The weak-stirring of scalar concentration process ensures that steep gradients persist at the boundaries of the cells, as shown in Fig. 25. Yet, as the flame front propagates, the vortex entrains the flame front over time by a sort of “homogenization” pro-

cess (i.e., by the synergy of differential rotation and diffusion) [37]. This explains why we still see the formation of the staircase in Fig 18.

From earlier analysis, we know that scalar concentration travels along contours of strong shear; therefore, we can use the Okubo-Weiss field to map the trajectory of the scalar concentration. To map the path of the scalar concentration in the Okubo-Weiss field, we connect regions of strong shear to their nearest strong shear neighbor, as shown in Fig. 27. Proof that the scalar travels along areas of strong shear is firmly established by comparing the paths found in the Okubo-Weiss

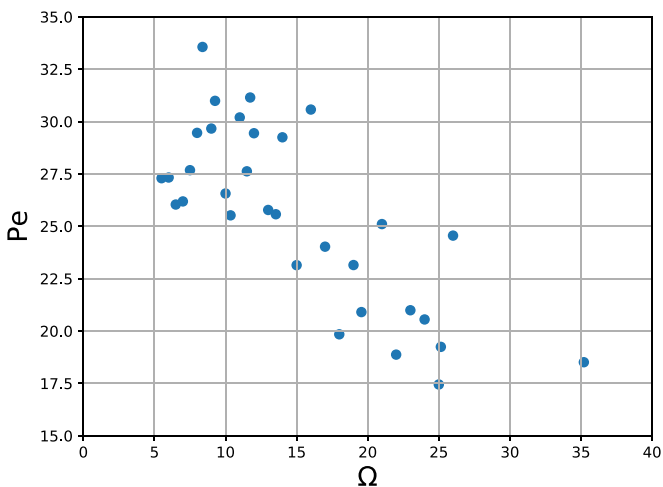


FIG. 23. Pelet number as a function of Ω . As the vortex array is allowed to fluctuate, the two disparate timescales change. Fluctuations of the cells weakens the cell mixing timescale.

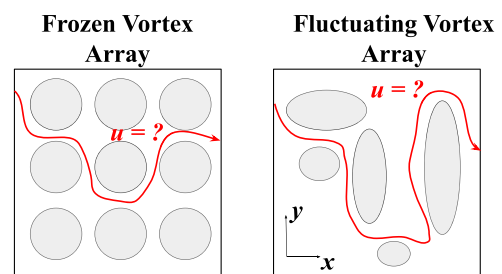


FIG. 24. The scalar concentration trajectory at various stages of the fluctuating vortex array. Its important to note that the scalar concentration trajectory is the path that an element of scalar concentration (i.e., scalar particle) takes to reach the right boundary. The solid curved (red) line represents the path of the scalar particle.

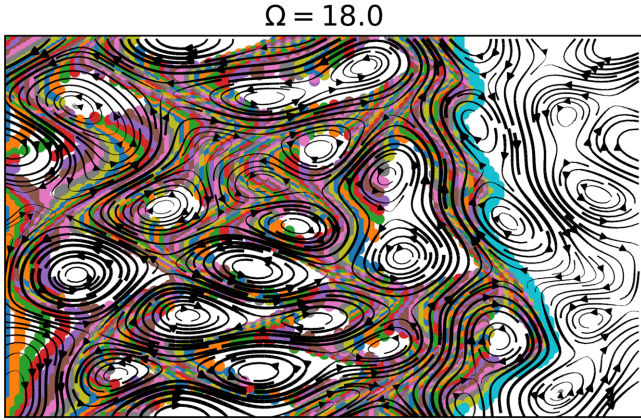


FIG. 25. In the process of forming a staircase structure, the scalar concentration first forms a “web.” The scalar concentration flows along areas of strong shear. The holes correspond to vortex structures. Here, the barriers are formed first because scalar concentration travels along regions of strong shear. Over time, scalar concentration slowly enters the vortices and becomes homogenized.

field to those in the scalar field. Here, it is significant to note that the scalar concentration travels along strong shear but not across it.

By mapping the scalar concentration trajectory, we learn how the vortex array affects the speed of the scalar concentration front propagation. Here, we use the map of the trajectory to determine the travel distance. The travel time is determined by the number of time steps required for the scalar concentration’s furthestmost point (in x) to reach the right boundary. While pulsing scalar concentration, we mark points (in green) on the scalar concentration contours (Fig. 26) when n attains a critical value ($n_{crit} = 0.1$). This enables us to quantify the travel time of the scalar concentration. We show the average scalar speed as a function of Ω in Fig. 28. The plot shows that the scattering of vortices leads to an overall decrease in scalar concentration velocity. An idea that is relevant here is the *least time criterion*. As the cellular array scatters, the

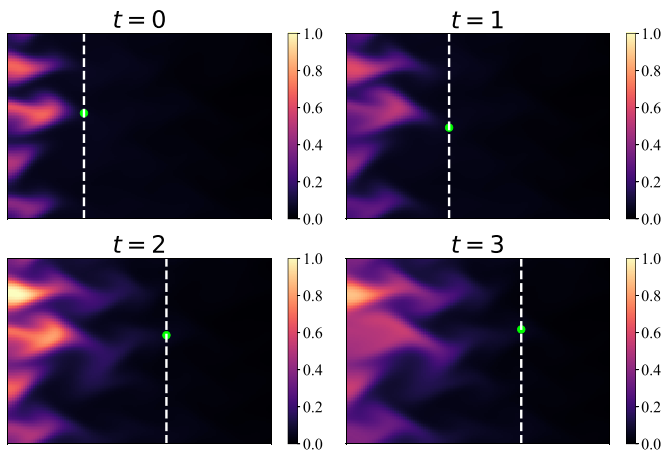


FIG. 26. Pulse train of scalar concentration in $\Omega = 11.5$ flow. Flame front propagates, over time vortex entrains flame front. At different times, we mark the position of $n_{crit} = 0.1$ in green (light gray).

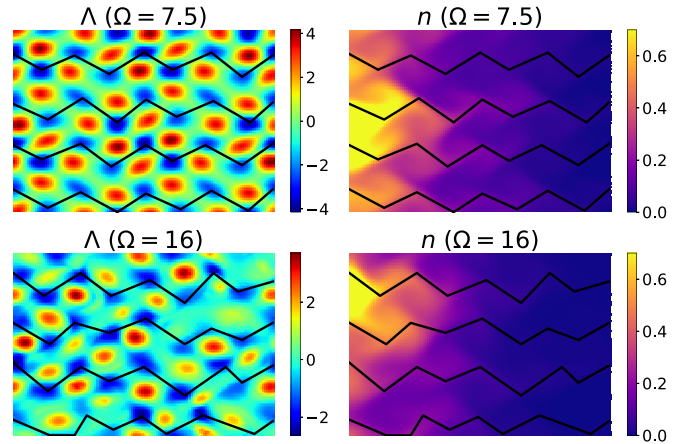


FIG. 27. In Okubo-Weiss field areas of strong shear ($\Lambda < 0$) are connected to their nearest strong shear neighbor. The connections in the Okubo-Weiss field are mapped to the scalar concentration contour to show that scalar concentration travels along areas of strong shear.

path of least time increases in length (similar to scattered path of light in atmosphere). We also find that the average scalar concentration front speed follows a similar trend to that of the staircase curvature plot as we increase Ω . We speculate that curvature may ultimately be related to the scalar concentration front speed,

$$\bar{u} \sim \frac{1}{\Omega^a},$$

$$\kappa \sim \frac{1}{\Omega^b}.$$

Here, a and b represent different constants. Therefore, $\bar{u} \sim \kappa^{a/b}$.

Finally, we investigate how the effective diffusivity for the relaxed vortex array differs from the fixed cellular array. Again, applying Fick’s law, we find that as the cells fluctuate, the effective diffusivity also fluctuates but remains close to

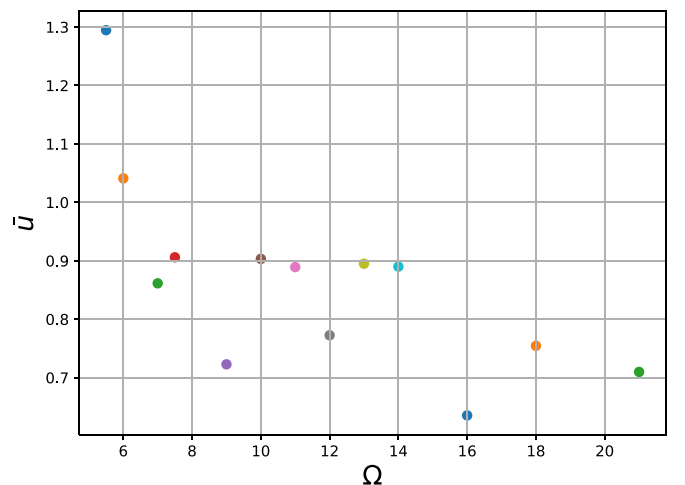


FIG. 28. Plot of the scalar front propagation speed as a function of Ω . The scattering of vortices leads to a decrease in front propagation speed. As the cellular array scatters, the path of least time increases in length.

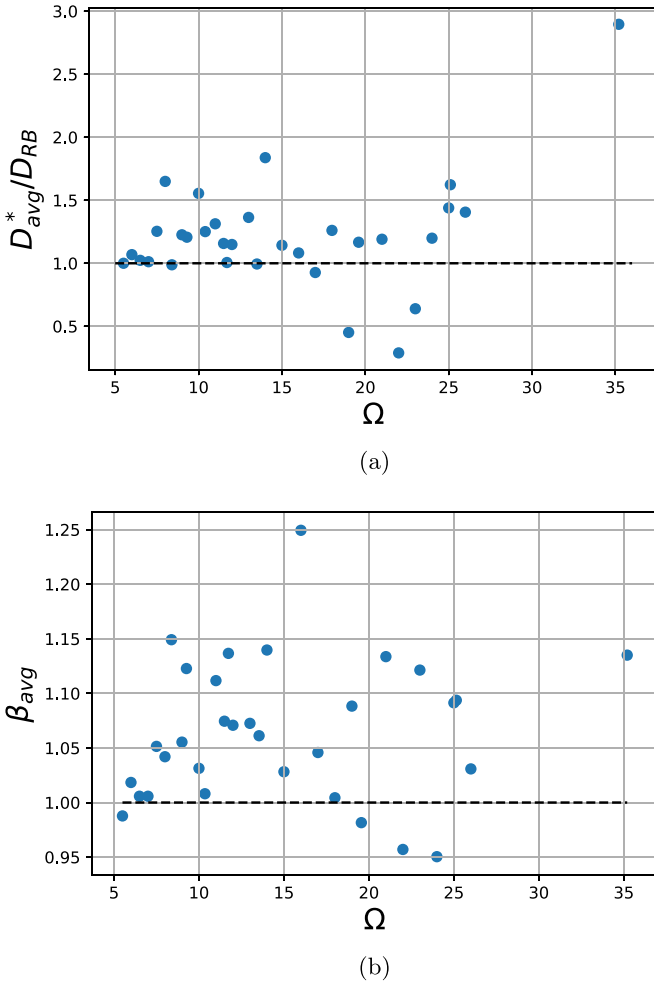


FIG. 29. Plot of effective diffusion (D^*) over the zero temperature effective diffusion (D_{RB}) as a function of Ω . The effective diffusion is shown to hug the line of 1, hence it does not deviate significantly from D_{RB} . The effective diffusivity is defined as $\propto D\sqrt{\text{Pe}}$. Keeping all quantities fixed, the only parameter that affects D^* is β , which corresponds to the ratio of the cell's length d_x/d_y . We see through (b) the direct effects that the geometrical properties of the cells has on the value of D^* .

the validated effective diffusivity [Eq. (4)]. We show this in Fig. 29(a). Note that we calculate D^* for the two orientations at points $x_1 = (1/4)L'$ and $x_2 = (3/4)L'$ using the method described in Appendix C. Although cell structures fluctuate, we note that as long as the cell boundaries are not destroyed, the transport across cell boundaries will not change. The reason for deviation in the effective diffusivity is due to geometrical properties of the cell structure and the cell turn-over velocity.

As mentioned in Sec. III A, all simulations ran in this experiment use a fixed background diffusivity; therefore, only cell dimensions and cell turn-over velocity ($0 < u_{\text{cell}} < \tilde{u}$) will determine the effective diffusivity. Based on the definition of Eq. (4), the only significant values in D_{cell} are d_x , d_y , and u_{cell} . Thus, we can define a scaling for the effective diffusion as

$$D^* \propto \sqrt{u_{\text{cell}} d_x \beta}, \quad (27)$$

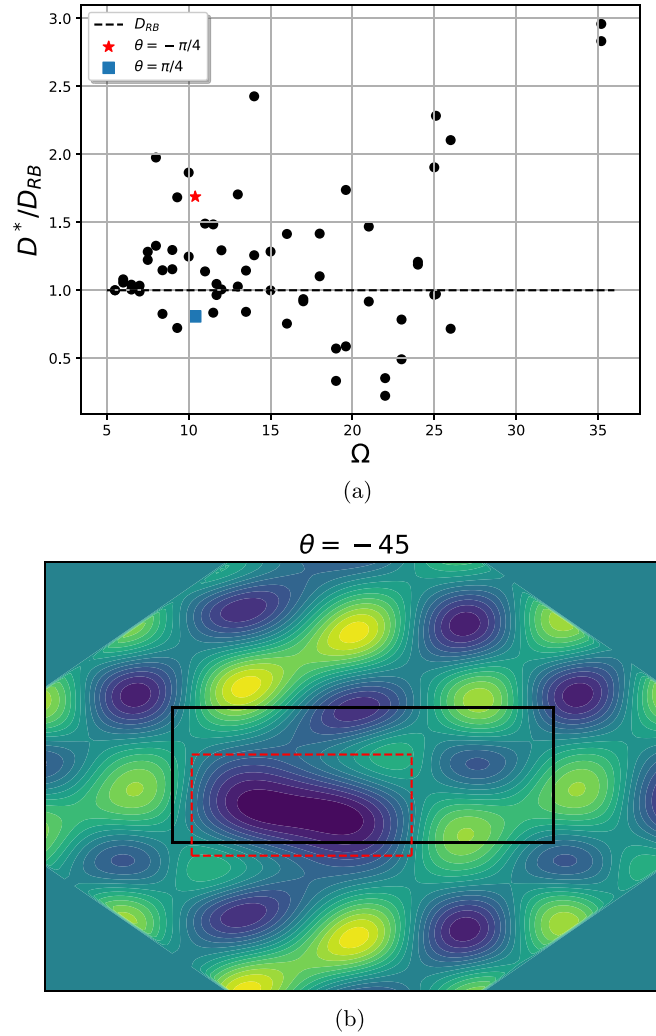


FIG. 30. The effective diffusion at different orientations as a function of Ω and the contour image of ψ at $\Omega = 10.35$ rotated at $\theta = -\pi/4$. The orientation of the dashed red boxed cell significantly influences the placement of D^* either below or above the dotted line.

where β is defined as d_x/d_y . As depicted in Fig. 13, the cells exhibit variations (both d_x and d_y change) with the incremental rise in the value of Ω . In this paper, we will examine the impact of d_x and d_y , as our emphasis is on the impact of cell geometry on pattern formation.

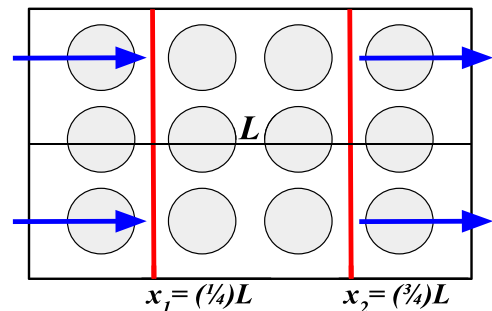


FIG. 31. Illustration of region we use to calculate D^* .

A plot of β as a function of Ω is shown in Fig. 29(b), which demonstrates similar characteristics to the effective diffusion plot. The β shown in the graph is an average of all cell sizes for each Ω ; nevertheless, the mean of the aspect ratio shows the direct effects the dimensions of the cells have on transport. If d_x is greater than d_y , then D^* will be greater than the effective diffusivity for the fixed cellular array, which we refer to as D_{RB} . If d_x is less than d_y , then the effective diffusivity is less than D_{RB} . We confirm this theory by analyzing the cellular flow at different orientations. We use $\Omega = 10.35$ to illustrate this point (see Fig. 30). As shown in Fig. 30, $\beta \sim 1$ is the average for the cells, but there are outliers (due to cell mergers) that make the average go above or below $\beta = 1$. This is a reason why D^* deviates somewhat from D_{RB} .

To assess the relationship between cell dimensions and D^* , we compute the correlation coefficient between Fig. 29(a) and its corresponding d_x^2/d_y value, which results in a value of 0.47. The computed value suggests a moderately positive correlation between cell dimensions and D^* . It is important to note that another factor to consider is the circulation speed of the cells in the region where D^* is measured. Given the variability in cell lengths, the cell turn-over velocity will also exhibit fluctuations, influencing the effective diffusivity. Nonetheless, our findings indicate that with knowledge of cell dimensions d_x and d_y , one can qualitatively approximate the trend of the effective diffusivity in a fluctuating vortex array.

IV. CONCLUSION

In this paper, we examine a minimal approach to layering to explore staircase resiliency and scalar concentration transport in a very simple system. The constrained cellular array, which produces layering as a consequence of two disparate timescales, is probed by introducing global transverse shear and turbulence-induced mixing in the cellular flow. It is important to note that there is no dynamic feedback necessary. Here, we summarize the principal results of this paper:

- (1) In an array of cells, the staircase structure forms in the presence of global transverse shear and turbulence-induced mixing. Each, of course, affects the staircase structure differently.
- (2) Global transverse shear introduces a shear dispersion timescale, which *enhances* the mixing of scalar concentration along y . This shear suppresses transport along x , resulting in an improvement in the confinement of scalar concentration.
- (3) Staircases form in the fluctuating vortex array over a broad range of modest Reynolds numbers ($0 < \Omega < 40$). N.B., regions of corrugations lessen, due to cell mergers. The staircases in the fluctuating vortex array satisfy the two criteria for resiliency, $Pe \gg 1$ and $\kappa \geq 1.5$.
- (4) Scalar concentration travels along regions of strong shear, creating a “web” structure. Here, staircase barriers form first, and scalar concentration “homogenizes” in vortices at a later time.
- (5) The scattering of vortices leads to an overall decrease in scalar concentration front velocity. The paths are those of the least time.
- (6) If background diffusion is kept fixed, then cell geometric properties can qualitatively approximate the trend of the

effective diffusivity. The effective diffusivity of the fluctuating vortex array does not deviate significantly from $D\sqrt{Pe}$.

The results of these simulations and their implications for a physical system, such as drift-wave turbulence near marginal stability in magnetic confinement devices, are reviewed and elucidated below.

The addition of a global transverse shear [Eq. (12)] to the fixed cellular array introduces a shear dispersion timescale, τ_{adv} . We find that for a critical shear strength [$\alpha m = 12\pi D/(\bar{u}d^2)$], the global transverse shear dissolves the staircase structure and increases $d\langle n \rangle_y/dx$. Therefore, transverse shear reduces the mixing of scalar concentration along the mean gradient (see Figs. 7 and 9). For shear strength values such that $\tau_S < \tau_H < \tau_D$, the mixing in y of scalar concentration can no longer be enhanced significantly regardless of the value of α and m . We summarize the different timescale orders and their corresponding range of αm values in Table I.

The problem presented in Ref. [23] and in the global shear flow section involves fixed ordered arrays. As mentioned in Sec. III, an actual physical system will manifest variability. Therefore, we introduced variability in the cellular array via forcing and drag in the NS equation [Eq. (17)] to study a less constrained cellular array. Here, Reynolds (Ω) and Ekman-friction (α) numbers control turbulent mixing and large-scale flows. By injecting scalar concentration into the relaxed cellular array, we find that the staircase is resilient to cell fluctuations. Our results indicate that staircase structures persist, though staircase steps become less regular due to cell mergers.

We established a set of criteria for the statement of “resiliency.” Two appropriate criteria for a staircase structure to be resilient are (1) $Pe \gg 1$ and (2) $\kappa \geq 1.5$. The first criterion is a fundamental requirement so that barriers are formed and maintained, and the second criterion establishes that a staircase should sustain a sufficient number of steps. For the range of $0 < \Omega < 40$, criterion (1) is satisfied. The second criterion is empirical and emerges from our studies. Over the relevant scope of Ω values, criterion (2) is maintained.

By closely analyzing the global structure of the scalar field, the scalar concentration first travels along regions of strong shear. This implies that staircase barriers form before “homogenization” takes place inside the vortices. The analysis is confirmed through the visualization of flame fronts in our simulations. Here, flame fronts occur in the regime of weak cell advection (Figs. 26 and 27).

In addition, by tracking the scalar concentration front in the flow, we determine the path and time it takes for an element of scalar concentration to travel along the mean gradient. We discover that as cells fluctuate, the scalar concentration path of least time *increases*.

Finally, we find that the effective diffusivity for the relaxed cellular array does not deviate significantly from that of the constrained cellular array [see Fig. 29(a)]. We find that as long as the boundaries and speed of the cells are maintained, the effective diffusivity and transport do not change. Since effective diffusivity is proportional to β , the transport of scalar concentration can change by modification of cell geometric properties (e.g., changing cell size d_x or d_y). We illustrate the effect of β on D^* in Fig. 29(b).

TABLE IV. Comparison of vortex array to drift-wave turbulence in fusion devices.

	Vortex field	Drift-wave turbulence (tokamak)
Inhomogeneity (free energy source)	∇n	$B_0, \nabla n,$ and ∇T
Reynolds number	$\Omega = 0-40$	$Re = 10^1-10^2$ (Landau Damping)
Flux	Scalar	Heat
Zonal Flow	Boundary layer between cells	$\mathbf{E} \times \mathbf{B}$ shear flow (poloidal)

These results have intriguing implications for experiments and theory. Our simulations show that the staircase structure is resilient in the regime of low-modest Reynolds numbers (i.e., steady fixed and spatiotemporal chaotic flow). For our model, low-modest Reynolds numbers indicate that flow properties are dominated by the forcing function (F_ω) as opposed to viscous forces. This regime is relevant to drift-wave turbulence, where effective Reynolds numbers range from 10–100. Here, the ratio of inverse correlation time to the Landau damping rate (i.e., nonlinear rate to the linear rate) can be used as a surrogate for the Reynolds number. We emphasize that in this system the dissipation is due to collisionless processes, such as Landau damping (which occurs due to wave-particle resonance), and not collisional viscosity [38]. For a comparison of the fluctuating vortex array model and drift-wave turbulence, see Table IV.

In addition to staircase resiliency, our findings suggest that if shear strain flows are stronger than vortical flows, the spatial propagation of turbulent intensity will travel along regions of saddles, thus initiating the formation of the staircase barriers. By studying the propagation of the turbulent intensity, we observe that fluctuating cellular flow hinders the speed of avalanche propagation. It is important to note that transport of turbulent intensity (i.e., turbulent spreading) and avalanching are closely related [39].

To conclude, we find that the effective diffusivity derived for the fixed cellular array is a suitable approximation for marginally overlapping cells in magnetic confinement. This result applies if one only considers changes in the geometric properties of the $\mathbf{E} \times \mathbf{B}$ convection cells. Results such as $D^* \approx \sqrt{DD_{\text{cell}}}$ may be relevant to magnetic confinement scenarios when conditions are similar to those of this study. The result argues that effective diffusivity is not a simple addition, but a geometric mean.

Results presented in this paper open the door to more complicated numerical simulations and experimental work, which can expand and change our understanding of inhomogeneous mixing. The first and most simple avenue to explore is the parameter space of $\tau_S \geq \tau_v$. In this scenario, fluid momentum diffusion occurs at a rate faster than the growth of large-scale flows. Thus, scalar concentration dynamics may differ from those found in this paper. A logical next step to explore is the effects of *active scalar* dynamics on the cellular array and inhomogeneous mixing. For those interested, we provide an introduction to the *active scalar* problem in Appendix D. Note that the active scalar problem is also relevant to the problem of liquid crystals, where waves in the director field behave like Alfvén waves.

Finally, due to the simplicity and generality of the problem, it is possible to test the theory presented here with actual experimental data. In the large linear magnetized plasma

device (LAPD), a vortex array can be created through modifications of a cathode plasma source with designer masks that form multiple current channels in a cellular pattern, thus forming the staircase structure [40–42]. This experiment will allow us to test hypotheses and models of staircase resiliency presented in this paper. In addition, the results of this experiment will yield a unique set of observations that can be used to test staircase models and impact the interpretation of experiments in other magnetically confined plasmas.

ACKNOWLEDGMENTS

The authors thank T. S. Hahm and D. W. Hughes for useful discussion and Rahul Pandit and Prasad Perlekar for sharing their work on the problem of the Melting Vortex Crystal. This inspired us to relate the melting process of the crystal to drift-wave turbulence. In addition, we thank Richard Sydora for leading the proposal of a detailed experimental test of results presented in this paper. We also acknowledge stimulating interactions with participants of the 2022 Transport Taskforce Workshop (TTF), Festival de Théorie 2022, and Asia-Pacific Conference on Plasma Physics (AAPPS-DPP) (2021, 2022). This research was supported by the U.S. Department of Energy under Award No. DE-FG02-04ER54738.

APPENDIX A: MAGNETIC CONFINEMENT MOTIVATION

A current subject of interest in magnetic confinement is the $\mathbf{E} \times \mathbf{B}$ staircase [7,10,43]. Nonequilibrium, near marginal plasmas can sometimes naturally evolve towards a globally organized critical state of spatially segregated micro barriers, interspersed between sectors of strong, avalanche-like transport [44–47]. The regime of “near marginality” is a relevant operating regime for present and future magnetic confinement devices. Here “marginality” refers to the normalized temperature gradient for which the turbulent heat flux exceeds neoclassical heat flux [48].

Evidence of the $\mathbf{E} \times \mathbf{B}$ staircase has been observed in current fusion devices [19,49–51] and simulations [9,52,53]. In simulations, the pressure profile plot shows the coexistence of profile flat spots and strong shear layers, which act as mini-barriers. The shear layers correspond to strongly localized temperature gradients. Avalanches occur in flat spots between shear layers and zonal flows (ZF) occur in the areas of mini-barriers. Note that ZF formation is the result of nonlocal interactions (in k -space) between unstable drift-wave modes. ZF are understood to regulate turbulence by “eddy shearing.”

Two ideas from self-organization that can explain the $\mathbf{E} \times \mathbf{B}$ staircase are $\mathbf{E} \times \mathbf{B}$ shear feedback and jams. The shear feedback process involves the zonal shears, turbulence, and

their mutual interaction by modulation processes. It is useful to view drift-wave turbulence and ZF as separate populations which interact via a “predator-prey” feedback loop: the drift waves (the prey) grow due to the gradient (instability) drive, while the ZF (the predator) “feed” upon the drift wave population by Reynolds stresses. For the case of jams, it is useful to draw inspiration from traffic flow theory, where time delay is the key element [19,20,54]. In traffic flow, a driver’s prompt (i.e., short) reaction maintains smooth traffic flow, while longer driver reaction times trigger jams [55]. In the case of flux-driven turbulence, heat flux jams occur when there is sufficient time delay between temperature modulations and local heat flux. This leads to the growth of patterns that resemble shock trains, from which develop the staircase “jumps.” Jumps here are simply the outcome of steepening the temperature gradient.

APPENDIX B: DERIVATION OF REYNOLDS NUMBER AND VORTEX EQUATION

The forced incompressible Navier-Stokes equation in 2D is of the form,

$$\frac{d\mathbf{u}'}{dt'} + \frac{\nabla' p'}{\rho} = \nu \nabla'^2 \mathbf{u}' - \alpha' \mathbf{u}' + F_{\text{amp}}(\sin ky' \hat{x} - \sin kx' \hat{y}), \quad (\text{B1})$$

where α' is the Ekman-friction and ν the kinematic viscosity. Here the density ρ is set to 1. This system has the solution,

$$\mathbf{u}' = \frac{F_{\text{amp}}}{k^2 \nu} (\sin ky' \hat{x} - \sin kx' \hat{y}). \quad (\text{B2})$$

To derive the Reynolds number for the forced NS equation, we use the maximum speed of Eq. (B2),

$$U_0 = \frac{F_{\text{amp}}}{k^2 \nu}. \quad (\text{B3})$$

For computational purposes, we chose the following normalization for position and time

$$\mathbf{x} = \frac{k}{n} \mathbf{x}', \quad (\text{B4})$$

$$t = \frac{F_{\text{amp}}}{nk\nu} t', \quad (\text{B5})$$

where n is the spatial frequency of the forcing. We can then normalize and take the curl of Eq. (B1) to derive the vorticity equation,

$$\frac{d}{dt} \omega = \frac{1}{\Omega} \nabla^2 \omega - \alpha \omega + F_\omega. \quad (\text{B6})$$

Here Ω represents the Reynolds number and α the non-dimensional Ekman friction. These two control parameters are defined by the following quantities:

$$\Omega = \frac{n F_{\text{amp}}}{k^3 \nu^2}, \quad (\text{B7})$$

$$\alpha = \frac{nk\alpha'}{F_{\text{amp}}}. \quad (\text{B8})$$

The forcing function F_ω is defined as

$$F_\omega = -\frac{n^3}{\Omega} (\cos nx + \cos ny). \quad (\text{B9})$$

A detailed analysis on Eq. (B1) can be found in Ref. [56].

APPENDIX C: EFFECTIVE DIFFUSIVITY (D^*) CALCULATION

We compute the value of D^* using

$$\langle \Gamma \rangle = -D^* \nabla \langle n \rangle_y. \quad (\text{C1})$$

The left-hand side represents the flux of scalar concentration through the region between $x_2 = (3/4)L$ and $x_1 = (1/4)L$ at different points in time, as illustrated in Fig. 31. Thus, we have the following equation:

$$\langle \Gamma \rangle = \frac{\Delta x}{\Delta t} (n_{\text{tot},t_f}(x = [x_1, x_2]) - n_{\text{tot},t_i}(x = [x_1, x_2])), \quad (\text{C2})$$

where Δx represents the difference between x_2 and x_1 . Note that Δt represents 8.3 diffusive cycles. Here, we define the diffusive timescale (τ_D) with length scale $d = \pi/3$. For the right-hand side of Eq. (C1), we use Eq. (10) to evaluate the value of $\langle n \rangle_y$ at the two points x_2 and x_1 at time t_f ,

$$\nabla \langle n \rangle_y = \frac{\langle n_{t_f}(x_2) \rangle_y - \langle n_{t_f}(x_1) \rangle_y}{\Delta x}. \quad (\text{C3})$$

By performing these calculations, we can compute a numerical value for D^* . Note that for the oblique staircase profiles, we replace the length L with L' .

APPENDIX D: ACTIVE SCALAR PROBLEM

For the active scalar problem, we convert the passive scalar (n) to an active scalar (A),

$$\left(\frac{\partial}{\partial t} + \mathbf{u} \cdot \nabla \right) A = \eta \nabla^2 A, \quad (\text{D1})$$

which will result in a system isomorphic to 2D MHD. Such systems are used to study flux expulsion [57,58] and vortex bursting [59]. Here, the active scalar is coupled to the vorticity equation, thus creating feedback. The governing vorticity equation will be of the form

$$\left(\frac{\partial}{\partial t} + \mathbf{u} \cdot \nabla \right) \omega = \frac{1}{\Omega} \nabla^2 \omega + \boxed{\mathbf{B} \cdot \nabla \nabla^2 A} + F_\omega - \alpha \omega, \quad (\text{D2})$$

$$\mathbf{B} = \hat{z} \times \nabla A. \quad (\text{D3})$$

We box the term, which couples the vorticity equation and Eq. (D1). For the active scalar, we consider an initial profile $A = B_0 x$, which results in a vertical magnetic field $B = B_0 \hat{y}$. Here, the value of B_0 plays a crucial role in how the active scalar impacts the dynamics of the flow. Depending on the magnitude of B_0 , the flow can be in a kinematic or dynamic regime. The regime is determined by

$$M = \left(\frac{v_A}{U_0} \right)^2 R_m. \quad (\text{D4})$$

The terms v_A and U_0 represent the Alfvén speed and the characteristic flow speed, respectively. Here R_m represents the magnetic Reynolds number. Note that v_A is proportional to B_0 , thus the strength of B_0 will determine the dynamics of the flow. First, we will discuss $M < 1$, the flux expulsion regime. For sufficiently small values of B_0 (i.e., $v_A^2 < U_0^2/R_m$), the vortex will expel magnetic field lines to the vortex boundary.

Due to magnetic field expulsion, the boundary layer of a cell will be reinforced, thus maintaining the cellular structure. In our cellular array model, we expect that the magnetic field will support the cell array structure when fluctuations are present (i.e., B_0 will elasticize the cell array). Since magnetic field lines are expelled to the boundaries, the active scalar essentially becomes homogenized ($\nabla A = 0$) inside the vortices, thus resulting in a staircase structure. Of course, unless the magnetic field is forced, the structure is only temporary since the magnetic field eventually decays in 2D.

The other case is the vortex bursting regime ($M > 1$). If B_0 is too large (i.e., $v_A^2 > U_0^2/R_m$), then vortices will be severely disrupted. In this scenario, Alfvénization takes place.

Alfvénization is the conversion of hydrodynamic turbulence to Alfvén wave turbulence. Thus, we expect that the formation of a staircase structure will not be possible. Until now, the problem of flux expulsion and vortex bursting has been addressed only in the context of a single eddy. To expand on this problem, we can use the setup of the vortex array, but now the vortices will be threaded by a magnetic field. In our upcoming study, we will address (through scans of B_0) what occurs to staircase dynamics. As magnetic fields get threaded around vortices, will this result in a more robust staircase? For what values of B_0 will the staircase structure no longer form? These are questions we plan to answer in the next phase of research.

-
- [1] D. G. Dritschel and M. E. McIntyre, Multiple jets as PV staircases: The Phillips effect and the resilience of Eddy-transport barriers, *J. Atmos. Sci.* **65**, 855 (2008).
- [2] P. Diamond, P. Garaud, D. Hughes, and B. Sutherland, KITP Program: Layering in Atmospheres, Oceans and Plasmas (2021), <https://online.kitp.ucsb.edu/online/staircase21/>.
- [3] D. W. Hughes and N. H. Brummell, Double-diffusive magnetic layering, *Astrophys. J.* **922**, 195 (2021).
- [4] T. Radko, Spin-down of a barotropic vortex by irregular small-scale topography, *J. Fluid Mech.* **944**, A5 (2022).
- [5] C. Caulfield, Layering, instabilities, and mixing in turbulent stratified flows, *Annu. Rev. Fluid Mech.* **53**, 113 (2021).
- [6] M. J. Choi, J. M. Kwon, L. Qi, P. H. Diamond, T. S. Hahm, H. Jhang, J. Kim, M. Leconte, H. S. Kim, B. H. Park, J. Chung, J. Lee, M. Kim, G. S. Yun, W. H. Ko, K. D. Lee, J. W. Juhn, and the KSTAR team, Dynamics and statistics of a self-organized electron temperature corrugation in KSTAR tokamak plasmas, in *Proceedings of the 6th Asia-Pacific Conference on Plasma Physics* (2022), <https://aapspdpp.org/DPP2022/html/3contents/pdf/topical/5391.pdf>.
- [7] G. Dif-Pradalier, G. Hornung, P. Ghendrih, Y. Sarazin, F. Clairet, L. Vermare, P. H. Diamond, J. Abiteboul, T. Cartier-Michaud, C. Ehrlacher, D. Estève, X. Garbet, V. Grandgirard, O. D. Gürcan, P. Hennequin, Y. Kosuga, G. Latu, P. Maget, P. Morel, C. Norscini *et al.*, Finding the elusive $E \times B$ staircase in magnetized plasmas, *Phys. Rev. Lett.* **114**, 085004 (2015).
- [8] P. G. Ivanov, A. A. Schekochihin, W. Dorland, A. R. Field, and F. I. Parra, Zonally dominated dynamics and Dimits threshold in curvature-driven ITG turbulence, *J. Plasma Phys.* **86**, 855860502 (2020).
- [9] W. Liu, Y. Chen, R. Ke, G. McKee, Z. Yan, K. Fang, Z. Yang, Z. Gao, Y. Tan, and G. R. Tynan, Evidence of $E \times B$ staircase in HL-2A L-mode tokamak discharges, *Phys. Plasmas* **28**, 012512 (2021).
- [10] G. Dif-Pradalier, G. Hornung, X. Garbet, P. Ghendrih, V. Grandgirard, G. Latu, and Y. Sarazin, The $E \times B$ staircase of magnetised plasmas, *Nucl. Fusion* **57**, 066026 (2017).
- [11] N. J. Balmforth, S. G. Llewellyn Smith, and W. R. Young, Dynamics of interfaces and layers in a stratified turbulent fluid, *J. Fluid Mech.* **355**, 329-358 (1998).
- [12] W. Guo, P. H. Diamond, D. W. Hughes, L. Wang, and A. Ashourvan, Scale selection and feedback loops for patterns in drift wave-zonal flow turbulence, *Plasma Phys. Control. Fusion* **61**, 105002 (2019).
- [13] P. B. Rhines, Waves and turbulence on a beta-plane, *J. Fluid Mech.* **69**, 417-443 (1975).
- [14] Y. Idomura, Self-organization in electron temperature gradient driven turbulence, *Phys. Plasmas* **13**, 080701 (2006).
- [15] A. Ashourvan and P. H. Diamond, How mesoscopic staircases condense to macroscopic barriers in confined plasma turbulence, *Phys. Rev. E* **94**, 051202(R) (2016).
- [16] A. Ashourvan and P. H. Diamond, On the emergence of macroscopic transport barriers from staircase structures, *Phys. Plasmas* **24**, 012305 (2017).
- [17] X. Garbet, O. Panico, R. Varennes, C. Gillot, G. Dif-Pradalier, Y. Sarazin, V. Grandgirard, P. Ghendrih, and L. Vermare, Wave trapping and $E \times B$ staircases, *Phys. Plasmas* **28**, 042302 (2021).
- [18] Q. Yan and P. H. Diamond, Staircase formation by resonant and non-resonant transport of potential vorticity, *Nucl. Fusion* **62**, 126032 (2022).
- [19] Y. Kosuga, P. H. Diamond, and O. D. Gürcan, How the propagation of heat-flux modulations triggers $e \times b$ flow pattern formation, *Phys. Rev. Lett.* **110**, 105002 (2013).
- [20] Y. Kosuga, D. Koga, and M. Sasaki, Numerical investigation on how heat flux avalanche jams trigger the staircase pattern formation, *Phys. Plasmas* **28**, 082302 (2021).
- [21] L. Qi, M. Choi, M. Leconte, T. Hahm, and J.-M. Kwon, Global $E \times B$ flow pattern formation and saturation, *Nucl. Fusion* **62**, 126025 (2022).
- [22] T. S. Hahm and P. H. Diamond, Mesoscopic transport events and the breakdown of Fick's law for turbulent fluxes, *J. Korean Phys. Soc.* **73**, 747 (2018).
- [23] M. N. Rosenbluth, H. L. Berk, I. Doxas, and W. Horton, Effective diffusion in laminar convective flows, *Phys. Fluids* **30**, 2636 (1987).
- [24] B. I. Shraiman, Diffusive transport in a Rayleigh-Bénard convection cell, *Phys. Rev. A* **36**, 261 (1987).
- [25] M. B. Isichenko, Percolation, statistical topography, and transport in random media, *Rev. Mod. Phys.* **64**, 961 (1992).
- [26] D. E. Newman, B. A. Carreras, P. H. Diamond, and T. S. Hahm, The dynamics of marginality and selforganized criticality as a paradigm for turbulent transport, *Phys. Plasmas* **3**, 1858 (1996).

- [27] P. Perlekar and R. Pandit, Turbulence-induced melting of a nonequilibrium vortex crystal in a forced thin fluid film, *New J. Phys.* **12**, 023033 (2010).
- [28] A. Gupta and R. Pandit, Melting of a nonequilibrium vortex crystal in a fluid film with polymers: Elastic versus fluid turbulence, *Phys. Rev. E* **95**, 033119 (2017).
- [29] A. Okubo, Horizontal dispersion of floatable particles in the vicinity of velocity singularities such as convergences, *Deep Sea Res. Ocean. Abstracts* **17**, 445 (1970).
- [30] J. Weiss, The dynamics of enstrophy transfer in two-dimensional hydrodynamics, *Physica D* **48**, 273 (1991).
- [31] A. Pocheau and F. Harambat, Front propagation in a laminar cellular flow: Shapes, velocities, and least time criterion, *Phys. Rev. E* **77**, 036304 (2008).
- [32] B. Audoly, H. Berestycki, and Y. Pomeau, Réaction diffusion en écoulement stationnaire rapide, *C. R. Acad. Sci., Ser. IIb: Mec., Phys., Chim., Astron.* **328**, 255 (2000).
- [33] M. Abel, A. Celani, D. Vergni, and A. Vulpiani, Front propagation in laminar flows, *Phys. Rev. E* **64**, 046307 (2001).
- [34] M. Abel, M. Cencini, D. Vergni, and A. Vulpiani, Front speed enhancement in cellular flows, *Chaos* **12**, 481 (2002).
- [35] N. Vladimirova, P. Constantin, A. Kiselev, O. Ruchayskiy, and L. Ryzhik, Flame enhancement and quenching in fluid flows, *Combust. Theory Model.* **7**, 487 (2003).
- [36] M. Cencini, A. Torcini, D. Vergni, and A. Vulpiani, Thin front propagation in steady and unsteady cellular flows, *Phys. Fluids* **15**, 679 (2003).
- [37] P. B. Rhines and W. R. Young, Homogenization of potential vorticity in planetary gyres, *J. Fluid Mech.* **122**, 347-367 (1982).
- [38] D. M. Meade, Physical mechanism for the collisionless drift wave instability, *Phys. Fluids* **12**, 947 (1969).
- [39] R. A. Heinonen and P. H. Diamond, Subcritical turbulence spreading and avalanche birth, *Phys. Plasmas* **26**, 030701 (2019).
- [40] B. Van Compernelle, W. Gekelman, P. Pribyl, and C. M. Cooper, Wave and transport studies utilizing dense plasma filaments generated with a lanthanum hexaboride cathode, *Phys. Plasmas* **18**, 123501 (2011).
- [41] R. D. Sydora, S. Karbasheski, B. Van Compernelle, G. Morales, and J. Maggs, Nonlinear convective heat transport in multiple interacting magnetized electron temperature filaments, in *Proceedings of the IEEE International Conference on Plasma Science (ICOPS'16)* (IEEE, Piscataway, NJ, 2016).
- [42] W. Gekelman, P. Pribyl, Z. Lucky, M. Drandell, D. Leneman, J. Maggs, S. Vincena, B. Van Compernelle, S. K. P. Tripathi, G. Morales, T. A. Carter, Y. Wang, and T. DeHaas, The upgraded large plasma device, a machine for studying frontier basic plasma physics, *Rev. Sci. Instrum.* **87**, 025105 (2016).
- [43] G. Dif-Pradalier, P. H. Diamond, V. Grandgirard, Y. Sarazin, J. Abiteboul, X. Garbet, P. Ghendrih, A. Strugarek, S. Ku, and C. S. Chang, On the validity of the local diffusive paradigm in turbulent plasma transport, *Phys. Rev. E* **82**, 025401(R) (2010).
- [44] B. A. Carreras, D. Newman, V. E. Lynch, and P. H. Diamond, A model realization of selforganized criticality for plasma confinement, *Phys. Plasmas* **3**, 2903 (1996).
- [45] Y. Sarazin and P. Ghendrih, Self-organized criticality in particle transport governed by ionization, *J. Nucl. Mater.* **241-243**, 322 (1997).
- [46] P. A. Politzer, Observation of avalanchelike phenomena in a magnetically confined plasma, *Phys. Rev. Lett.* **84**, 1192 (2000).
- [47] P. A. Politzer, M. E. Austin, M. Gilmore, G. R. McKee, T. L. Rhodes, C. X. Yu, E. J. Doyle, T. E. Evans, and R. A. Moyere, Characterization of avalanche-like events in a confined plasma, *Phys. Plasmas* **9**, 1962 (2002).
- [48] P. H. Diamond and T. S. Hahm, On the dynamics of turbulent transport near marginal stability, *Phys. Plasmas* **2**, 3640 (1995).
- [49] M. J. Choi, J.-M. Kwon, L. Qi, P. H. Diamond, T. S. Hahm, H. Jhang, J. Kim, M. Leconte, H.-S. Kim, J. Kang, B.-H. Park, J. Chung, J. Lee, M. Kim, G. S. Yun, Y. U. Nam, J. Kim, W.-H. Ko, K. D. Lee, J. W. Juhn, and the KSTAR team, The $E \times B$ staircase as the self-organization in the tokamak avalanche plasma, [arXiv:2207.06610](https://arxiv.org/abs/2207.06610).
- [50] M. J. Choi, H. Jhang, J.-M. Kwon, J. Chung, M. Woo, L. Qi, S. Ko, T.-S. Hahm, H. K. Park, H.-S. Kim, J. Kang, J. Lee, M. Kim, G. S. Yun, and the KSTAR Team, Experimental observation of the non-diffusive avalanche-like electron heat transport events and their dynamical interaction with the shear flow structure, *Nucl. Fusion* **59**, 086027 (2019).
- [51] A. Ashourvan, R. Nazikian, E. Belli, J. Candy, D. Eldon, B. A. Grierson, W. Guttenfelder, S. R. Haskey, C. Lasnier, G. R. McKee, and C. C. Petty, Formation of a high pressure staircase pedestal with suppressed edge localized modes in the DIII-D tokamak, *Phys. Rev. Lett.* **123**, 115001 (2019).
- [52] G. Hornung, G. Dif-Pradalier, F. Clairet, Y. Sarazin, R. Sabot, P. Hennequin, and G. Verdoolaege, Staircases and barrier permeability in magnetised plasmas, *Nucl. Fusion* **57**, 014006 (2017).
- [53] F. Rath, A. G. Peeters, and A. Weikl, Analysis of zonal flow pattern formation and the modification of staircase states by electron dynamics in gyrokinetic near marginal turbulence, *Phys. Plasmas* **28**, 072305 (2021).
- [54] W. Wang, Y. Kishimoto, K. Imadera, J. Li, and Z. Wang, A mechanism for the formation and sustainment of the self-organized global profile and $E \times B$ staircase in tokamak plasmas, *Nucl. Fusion* **58**, 056005 (2018).
- [55] G. Whitham, *Linear and Nonlinear Waves* (Wiley-Interscience, New York, NY, 1999).
- [56] N. Platt, L. Sirovich, and N. Fitzmaurice, An investigation of chaotic Kolmogorov flows, *Phys. Fluids* **3**, 681 (1991).
- [57] N. O. Weiss and J. B. Adams, The expulsion of magnetic flux by eddies, *Proc. R. Soc. London A* **293**, 310 (1966).
- [58] H. Moffatt and H. Kamkar, On the time-scale associated with flux expulsion, in *Stellar and Planetary Magnetism*, edited by A. M. Soward (Gordon & Breach Science Publishers Ltd, 1983), pp. 91-97.
- [59] J. Mak, S. D. Griffiths, and D. W. Hughes, Vortex disruption by magnetohydrodynamic feedback, *Phys. Rev. Fluids* **2**, 113701 (2017).